Article

Slipknot-gauged mechanical transmission and robotic operation

https://doi.org/10.1038/s41586-025-09673-w

Received: 25 June 2024

Accepted: 25 September 2025

Published online: 26 November 2025

Open access

Check for updates

Yaoting Xue[1,15], Jiasheng Cao[1,2,15], Tao Feng[1,15], Kaihang Zhang[1,15], Siyang Li[1], Jiahao Hu[2,3], Haotian Guo[1,4], Jinming Zhang[2,5], Yaoxian Song[1], Zhuofan Wang[1], Lei Wang[1], Qishan Huang[1], Haofei Zhou[1], Fanghao Zhou[1,6,7], Jiliang Shen[2], Yaowei Fan[1], Zhe Wang[1], Xinge Li[1,6], Jie-Wei Wong[1], Zhiwei Chen[8], Dongrui Ruan[1], Zhikun Miao[1], Bin Zhang[2], Enjie Zhou[2], Letian Gan[1], Xuanqi Wang[1], Ertai Cao[1], Tong Chen[1], Weifeng Zou[1], Junhui Zhang[8], Haojian Lu[9], Qinghai Zhang[7,10], Song Liu[11], Huixu Dong[4], Shiying Xiong[1], Shuyou Peng[2,12], Tuck-Whye Wong[1], Yuanjie Chen[13,14], Tiefeng Li[1,5,6,7,8] ✉, Mingyu Chen[2,3] ✉, Xuxu Yang[1] ✉, Wei Yang[1] ✉ & Xiujun Cai[2,3] ✉

Mechanical transmission is essential in force-related activities ranging from the daily tying of shoe laces[1] to sophisticated surgical[2] and robotic operations[3,4]. Modern machines and robots typically use complex electronic devices designed to sense and limit force[5], some of which still face challenges when operating space is limited (for example, in minimally invasive surgeries)[6] or when resources are scarce (for example, operations in remote areas without electricity). Here we describe an alternative slipknot-based mechanical transmission mechanism to control the intelligent operation of both human and robotic systems. Through topological design, slipknot tying and release can encode and deliver force with a consistency of 95.4% in repeating operations, which circumvents the need for additional sensors and controllers. When applied to surgical repair, this mechanism helped inexperienced surgeons to improve their knotting-force precision by 121%, enabling them to perform surgical knots as good as those of experienced surgeons. Moreover, blood supply and tissue healing after surgery were improved. The mechano-intelligence exhibited in slipknots may inspire investigations of knotted structures across multiple length scales. This slipknot-gauged mechanical transmission strategy can be widely deployed, opening up opportunities for resource-limited healthcare, science education and field exploration.

Mechanical transmission is integral to a wide range of force-related activities, from daily tasks to advanced surgical and robotic procedures[1–5]. Despite their importance, electronic force-sensing devices face challenges in environments with constrained space or limited resources, such as minimally invasive surgeries and off-grid operations[6], respectively. In surgical practice, explicit measurements of tension remain difficult, as sensing systems are often impractical to implement. Consequently, surgeons typically rely on visual estimation based on the degree of tissue deformation rather than on quantitative assessments[7]. To overcome such challenges, here we propose a slipknot-gauged mechanical transmission strategy that enables intelligent control for both human and robotic systems (Fig. 1a). Although topologically equivalent to trivial knots[8], the slipknot possesses distinct geometric and mechanical properties. Specifically, during its deployment, a sequence of peak force signals, denoted as F_{peak}, can be transmitted to the robot arm and human hand. Each slipknot is fabricated through a knot-tying process, whereby a pair of tensile forces are imposed on the string until a predefined value, denoted as F_{tying}, is reached (Fig. 1b, top left). This predefined tensile force can affect contact[9,10], friction[11] and elastic deformation[12,13] of the slipknot system (Fig. 1b, top right). To transmit the encoded force, a pair of forces are imposed on the free ends of the string (Fig. 1b, middle), which leads to a topology-preserving movement (Fig. 1b, bottom left) and final opening of the slipknot (Fig. 1b, bottom right). By analysing elastic deformation of the slipknot, the peak force, F_{peak} during the slipknot-releasing process can be quantified (Fig. 1b, bottom right). The robustness and consistency of the slipknot-gauged mechanical transmission strategy (Fig. 1c–e) was evaluated through a series of microrobotic operation experiments (Fig. 1c) and industrial robotic arm manipulations (Fig. 1d). The force encoding and releasing

[1]Center for X-Mechanics, Department of Engineering Mechanics, Zhejiang University, Hangzhou, China. [2]Department of General Surgery, Sir Run Run Shaw Hospital, Zhejiang University School of Medicine, Hangzhou, China. [3]National Engineering Research Center of Innovation and Application of Minimally Invasive Instruments, Hangzhou, China. [4]Grasp Lab, School of Mechanical Engineering, Zhejiang University, Hangzhou, China. [5]First Affiliated Hospital of Zhejiang University, Zhejiang University School of Medicine, Hangzhou, China. [6]State Key Laboratory of Ocean Sensing, Zhejiang University, Hangzhou, China. [7]Institute of Fundamental and Transdisciplinary Research, Zhejiang University, Hangzhou, China. [8]State Key Laboratory of Fluid Power and Mechatronic Systems, Zhejiang University, Hangzhou, China. [9]Institute of Cyber-Systems and Control, Zhejiang University, Hangzhou, China. [10]School of Mathematical Sciences, Zhejiang University, Hangzhou, China. [11]School of Information Science and Technology, ShanghaiTech University, Shanghai, China. [12]Department of General Surgery, the Second Affiliated Hospital, Zhejiang University, Hangzhou, China. [13]Zhejiang Institute of Quality Science, Hangzhou, China. [14]Zhejiang Provincial Key Laboratory of Digital Precision Measurement Technology, Hangzhou, China. [15]These authors contributed equally: Yaoting Xue, Jiasheng Cao, Tao Feng, Kaihang Zhang. ✉e-mail: litiefeng@zju.edu.cn; mychen@zju.edu.cn; xxyang@zju.edu.cn; yangw@zju.edu.cn; srrsh_cxj@zju.edu.cn

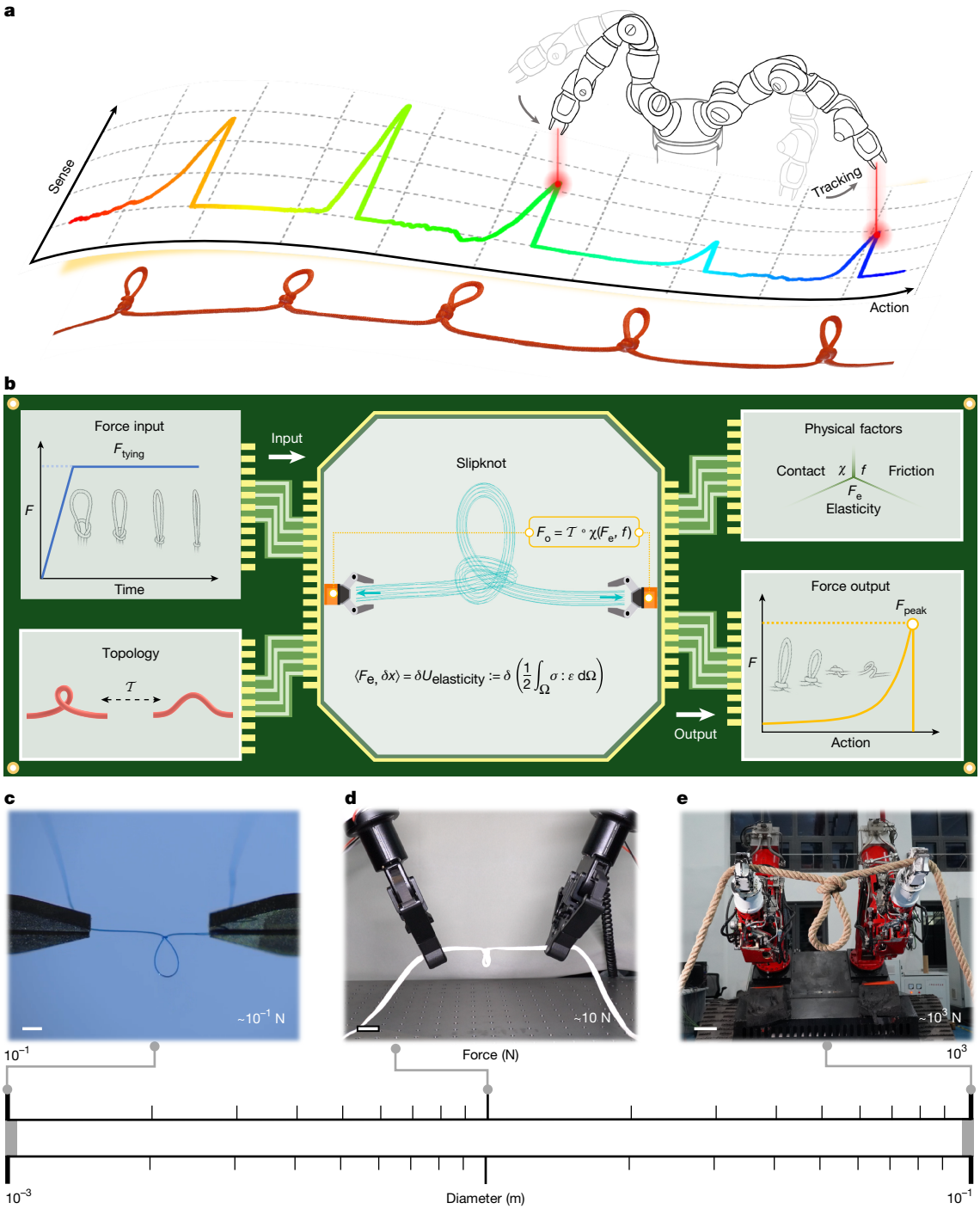

Fig. 1 | Schematic of mechanical information transmission in a string by slipknots. a, Schematic of a series of slipknots on a string that transmit force signal spectra to gauge robotic arm operations. **b**, The process of mechanical information writing and reading in a slipknot. Mechanical information is written into a slipknot by tying it with a specific force input. The mechanical model processes this force input, incorporating features such as physical factors and topology. The mechanical information is then output as the peak force, F_{peak}, during the knot-releasing process of pulling the slipknot. **c**–**e**, The slipknot-gauged mechanical transmission strategy was validated in scenarios including micro-operations (**c**), collaborative manipulation (**d**) and heavy-load rescue missions (**e**). Scale bars, 1 mm (**c**), 2 cm (**d**) or 10 cm (**e**).

mechanisms of slipknots were also validated in heavy-duty robotic operations (Fig. 1e).

Mechanical modelling and characterization of slipknots

We performed a tensile test on a filament with a typical slipknot, which was obtained using a pre-tightening force of F_{tying} = 7.500 N (Extended Data Fig. 1). High-speed photography (Supplementary Video 1) and microcomputed tomography (micro-CT) scanning techniques were used to capture the evolution of knot configurations (Fig. 2a,b). The initial configuration of the slipknot comprised two free ends, a knot loop and a slip loop (Fig. 2a, left). As the external force imposed on the free ends increased, the length of the slip loop gradually reduced (Fig. 2a–c, left four images). The force–displacement curve (Fig. 2d) showed a steady tensile force during the initial stage (Fig. 2d, (1) and (2)). Subsequently, the tensile force started to increase, which was caused

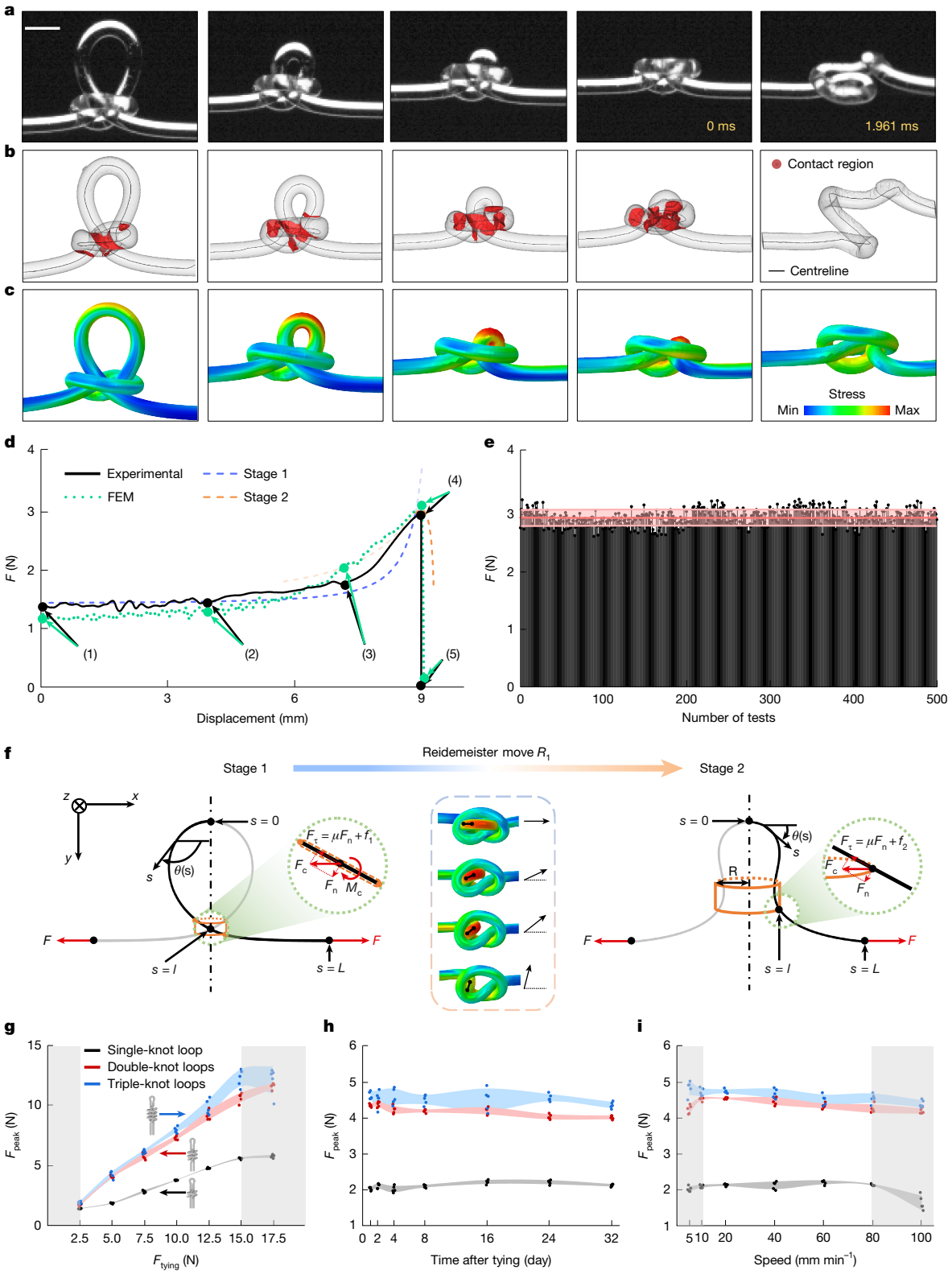

Fig. 2 | Mechanical modelling and characterization of slipknots. **a**–**c**, Snapshots of an opening slipknot by high-speed photography (**a**), micro-CT scanning (**b**) and finite element result (**c**). Scale bars, 1 mm. The slipknot transitions slowly from the initial state (first column) to the snap-out state (fourth column) when the first Reidemeister move, R_1, occurs and then rapidly opens (last column). **d**, Experimental and modelled (both theoretical and numerical) force–displacement curves of a slipknot. The theoretical model involves two stages: before (stage 1) and after (stage 2) the R_1 move. **e**, F_{peak} values of 500 slipknots on a fluorocarbon filament string tied with F_{tying} = 7.500 N. The values are located within 2.945 ± 0.135 N (mean ± s.d., n = 500 independent samples), showing a consistency of 95.4%. **f**, Mechanical model of the two stages before and after the R_1 move. Black and grey lines denote the rod part, and orange tubes indicate the constraint. Inset, the R_1 move in a simulation. **g**, Experimentally tested F_{peak} values (mean ± s.d.) in different configurations of single-knot, double-knot and triple-knot loops (n = 5 independent samples). **h**,**i**, F_{peak} changes over time (**h**) (mean ± s.d., n = 5 independent samples) and testing speed (**i**) (mean ± s.d., n = 5 independent samples) validate the stability of the slipknots in long-term and dynamic tests. Points in the figures denote experimental data, lines indicate mean values and shading reflects the uncertainty. Grey areas in these figures represent the unstable regions.

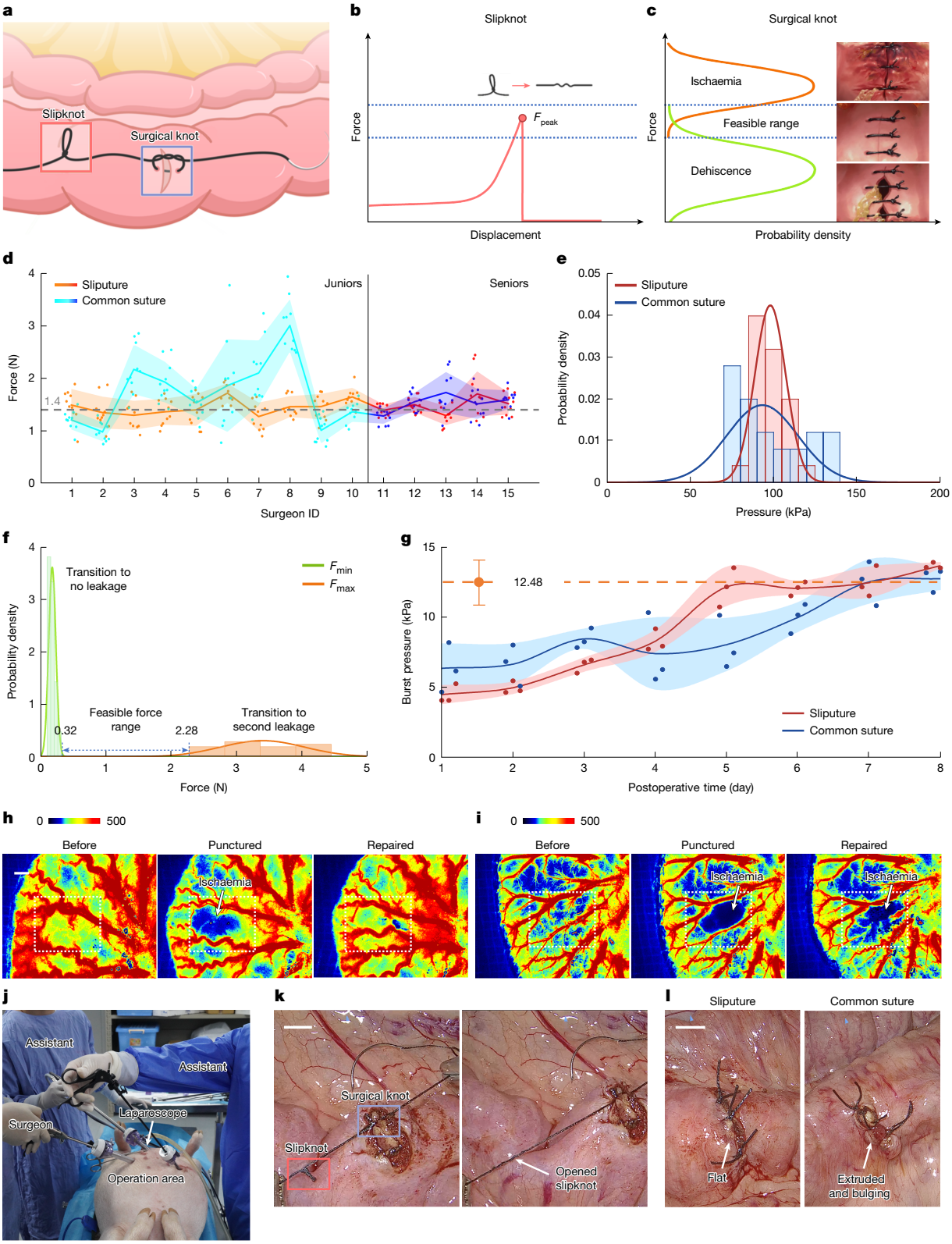

Fig. 3 | See next page for caption.

by an increase in writhe[14] (Fig. 2a, middle, d, (2–4)) and the stress concentration (Fig. 2c (left four images) and Supplementary Note 1) of the slip loop. Micro-CT scanning results revealed that the contact area between the slip loop and the knot loop also increased (Fig. 2b, left four images). After a critical force of F_{peak} = 2.931 N, the slip loop exhibited evidence that it was about to snap out[15] of the knot loop (Fig. 2a, fourth image), accompanied by topological Reidemeister moves[8] of the knot (Supplementary Fig. 1). After the slipknot fully opened up (Fig. 2a,b, far right images), the tensile force on the free ends rapidly declined, which was characterized by a sudden load drop (Fig. 2d, right two images) and stress release in the slip loop (Fig. 2c, far right image). The value of F_{peak} measured from tensile tests on 500 slipknots

Fig. 3 | A slipknot gauges mechanical transmission in surgical operations. **a**, A suture with a slipknot (red box) transmits a pre-encoded force to a surgical knot (blue box), termed a sliputure. **b**, The F_{peak} emerges at slipknot opening to transmit mechanical information. **c**, The F_{peak} is transmitted to the surgical knot during tying. A proper tying force within a feasible range produced a flat wound closure (middle image). Conversely, excessive force causes ischaemia (top image), whereas insufficient force leads to leakage (bottom image). **d**, The knot-tying force (mean ± s.d.; ribbons indicate the s.d.) of junior surgeons (n = 10; independent participants) and senior surgeons (n = 5; independent participants) (n = 10; independent experiments). With common sutures, junior surgeons showed lower force precision. Using sliputures without training significantly improved the precision of junior surgeons, even surpassing senior surgeons using common sutures. **e**, The probability density of the incision pressure is more compact with sliputures (n = 25; independent experiments). **f**, Feasible force range (n = 20; independent biological replicates) (blue) of ex vivo rat colonic injury repair was defined by F_{min} (green, transition to no leakage) and F_{max} (orange, transition to secondary leakage). **g**, Burst pressure (mean ± s.d.; ribbons indicate the s.d.) shows that sliputures produce initially lower pressures but plateau beyond controls after day 5, 2 days earlier (n = 3; independent biological replicates) than for common sutures. **h**,**i**, LSCI images of vessel visualization of rat colons after biopsy puncture and repair using sliputures (**h**) or common sutures (**i**). Dashed boxes mark punctured areas, which show that sliputures lead to improved blood supply. Colour bars represent relative perfusion units. **j**, Image of surgeons operating using the sliputure with laparoscopic instruments. **k**, The tying process with sliputures in laparoscopic repair of colonic injuries in live pigs. **l**, The repaired porcine colon regions by laparoscopic surgery appear flat when repaired using sliputures (left), whereas they appear bulging when repaired with common sutures (right). Scale bars, 1 mm (**h**) or 5 mm (**k**,**l**).

(Fig. 2e) was 2.945 ± 0.135 N, a result that highlights the consistency of slipknot-gauged mechanical transmission.

On the basis of the results obtained from experiments and simulations, particularly the importance of the Reidemeister move[16], we divided the process of slipknot release into two stages: stage 1 and stage 2 (Fig. 2f). Stage 1 comprises the release process before the Reidemeister move, whereby the tensile force increases owing to the combined effects of contact, friction and elasticity. Stage 2 consists of bifurcation due to additional Reidemeister movements, which leads to the F_{peak} and to further decreases in the tensile force (Supplementary Note 2). The interception point of the corresponding force–displacement curves was located immediately preceding the F_{peak}, which fits well with the experimental and simulation results (Fig. 2d and Supplementary Video 2).

Increasing the pre-tightening force F_{tying} and the number of knot loops when creating the slipknot enlarged the contact area between the slip loop and the knot loop (Supplementary Fig. 2), which provided a method to tune the F_{peak} (Fig. 2g). Under the same F_{tying} value, the F_{peak} could be modified through the use of monofilaments with different diameters (Extended Data Fig. 2). Slipknots made from different materials and structures also exhibited different friction coefficients when submerged in various liquid media (Extended Data Fig. 3 and Supplementary Note 3). These modifications subsequently affected F_{peak} values, which aligned with model predictions (Extended Data Fig. 4). Of note, slipknots retained their performance after 32 days of storage. Together, these results demonstrate the long-term mechanical stability of slipknots from production to practical use (Fig. 2h). Dynamic behaviour analyses revealed a nearly constant value of F_{peak} across a wide range of testing speeds (Fig. 2i). Such stability indicates that slipknots can reliably gauge operations that are either manually or mechanically driven.

A slipknot gauges mechanical transmission in surgical operations

Knot tying, the gold-standard procedure for closing incisions in surgery, requires the interplay of dexterity, expertise and experience of the surgeon[17,18]. The precise and robust mechanical transmission provided by a slipknot matches the demands for accuracy and consistency required in surgery[19] (Fig. 3a–c). In gastrointestinal surgery[20], for example, the maintenance of a suitable suturing force is challenging (Fig. 3c, middle). Failure of a surgical knot in gastrointestinal surgery can result in anastomotic leaks, which can lead to an increase in mortality of more than 30%[21]. Moreover, excessive force from tight knots can cause tissue ischaemia (Fig. 3c, top), whereas insufficient force from loose knots can result in dehiscence[22] (Fig. 3c, bottom). In contrast to alternatives such as modified suture materials[23] or the use of sutureless sealants[24], we propose that a slipknot (Fig. 3a, red box) can be connected in series at the end of a common suture (Fig. 3a, blue box) to form a new type of suture, termed the 'sliputure'. For surgeons, the required steps to perform a sliputure are as simple as tying the surgical knot as usual[18] and then pulling the slipknot until it opens. The pre-encoded opening force (F_{peak}) of the sliputure guarantees that the tying force of the surgical knot precisely aligns within the feasible range ($F_{surgical\ knot\ tying} = F_{peak}$) (Fig. 3b). Consistently good surgical suturing is typically gained through experience by the surgeon. Sliputure enables precise and robust control of the intelligent force limit without the need to alter established surgical practices or introduce additional devices. To test the sliputure system, we recruited surgeons with varying experience (more than 10 years (seniors) or fewer than 10 years (juniors)) and asked them to tie a surgeon's knot to close an incision on a silicone model (Supplementary Figs. 3 and 4). Using the common suture, a force of 1.534 ± 0.283 N (relative standard deviation of $V_\sigma^{Seniors,\ common\ suture}$ = 0.184) was measured when knot tying was performed by senior surgeons. Senior surgeons also exhibited higher precision than junior surgeons (1.716 ± 0.736 N, $V_\sigma^{Juniors,\ common\ suture}$ = 0.429). To expand the comparison of performance between junior and senior surgeons with sliputures, we introduced $|\Delta F|$, defined as the absolute difference between the actual and target F_{peak}. Notably, using a sliputure with a target F_{peak} of 1.400 N (F_{tying} = 0.350 N), junior surgeons exhibited better performance than with the common suture (1.445 ± 0.280 N, $V_\sigma^{Juniors,\ sliputure}$ = 0.194; $|\Delta F|_{Juniors,\ sliputure}$ = 0.238 ± 0.151 N compared with $|\Delta F|_{Juniors,\ common\ suture}$ = 0.575 ± 0.556 N, $P < 0.001$). By contrast, no significant difference was shown with senior surgeons (1.480 ± 0.272 N, $V_\sigma^{Seniors,\ sliputure}$ = 0.184; $|\Delta F|_{Seniors,\ sliputure}$ = 0.197 ± 0.201 N compared with $|\Delta F|_{Seniors,\ common\ suture}$ = 0.236 ± 0.204 N, P = 0.349). Furthermore, junior surgeons using sliputures achieved equivalent performance to senior surgeons using sliputures (P = 0.165) and common sutures (P = 0.927) (Fig. 3d). Compared with the common suture, sliputure improved the knotting force precision by 121% in junior surgeons. We next used a pressure-sensitive film to measure the incision pressure after suturing (Supplementary Fig. 3b). The probability density distribution of the pressure associated with sliputures (98.0 ± 9.6 kPa, relative standard deviation of $V_\sigma^{Sliputure}$ = 0.098) was more compact than with common sutures (93.2 ± 21.9 kPa, $V_\sigma^{Common\ suture}$ = 0.235) (Fig. 3e and Supplementary Video 3).

With precise and consistent force transmission, the slipknot-gauged intelligent operation had an immediate effect on clinical practice, as demonstrated using a rat model of colonic injury repair. The optimal knot-tying force to repair a colonic injury in rats ranged between 0.32 N and 2.28 N (Fig. 3f, Supplementary Fig. 5 and Supplementary Video 4). Note that the optimal knot-tying force for other surgical procedures can be obtained through combinations of experimental tests and mechanical modelling. Here we selected the midpoint, 1.30 N, as the target knot-tying force for subsequent experiments, and set F_{peak} = 1.300 N for the sliputure. The sliputure exhibited high force accuracy and efficacy in repairing both ex vivo (Supplementary Video 5) and in vivo (Supplementary Video 6) rat models of colonic

injury (Supplementary Fig. 6). Laser speckle contrast imaging (LSCI) showed that colonic injuries repaired with sliputures exhibited better restoration of the blood supply than those repaired with common sutures (Fig. 3h,i). Regarding surgery-related complications, sliputure-treated animals did not show macroscopic colonic leaks compared with common-suture-treated animals (0 out of 10 leaks compared with 2 out of 10 leaks, respectively, $P = 0.474$). Moreover, fewer postsurgical adhesions appeared after using sliputures than common sutures (3 out of 10 adhesions compared with 10 out of 10 adhesions, respectively, $P = 0.003$) (Supplementary Fig. 7). We evaluated healing of the colon by monitoring the burst pressure (Supplementary Fig. 8). Irrespective of the expertise of the surgeon, the slipknot-gauged mechanical transmission in the sliputure led to accelerated tissue healing. The burst pressure in the sliputure-treated group reached a healthy level by the fifth postoperative day, 2 days earlier than that in the common-suture-treated group (Fig. 3g). We evaluated wound healing of repaired tissues, which were collected on the fifth postoperative day, through haematoxylin and eosin (H&E) staining of samples to evaluate tissue recovery and through multiplex immunofluorescence staining to detect macrophage cell infiltration (CD86 and CD206) (Supplementary Fig. 9). Muscular layer continuity and restoration of mucosal glands correlated with a healed colon in the sliputure-treated group (Supplementary Fig. 9a). Analyses of cells labelled with the markers CD86 and CD206, which denote pro-inflammatory and anti-inflammatory macrophages, respectively, showed that the sliputure-treated group exhibited a notably increased anti-inflammatory trend in the repaired colon. This result demonstrates the enhanced recovery capacity of the sliputure (Supplementary Fig. 9b). Additional blood analyses of inflammation cells and comprehensive blood chemistry profiles indicated negligible systemic effects, thereby confirming the biocompatibility of the sliputure (Supplementary Fig. 10).

We further applied the sliputure to assist in laparoscopic surgery, whereby force feedback techniques are mostly used in simulation training rather than real surgical settings[25,26]. Here a pig model with colonic injuries was used to test the system. The surgeon operated the sliputure with straight rod-shaped laparoscopic instruments (Fig. 3j,k), which can transmit the force signal during slipknot opening back to the surgeon (Supplementary Video 7). Colonic injuries repaired using sliputures generally exhibited a flat appearance, whereas tissue extrusion and bulging were observed when common sutures were used (Fig. 3l). These results validate the performance of the sliputure in laparoscopic surgery. To quantify the benefits of the sliputure, we performed surgical suturing on a silicone practice model under a laparoscopic setup (Extended Data Fig. 5a–c and Supplementary Video 8). The results of measured pressures of incision showed that sliputures improved suturing precision by 71.3% compared with common sutures (103.2 ± 5.6 kPa, $V_\sigma^{\text{Sliputure}} = 0.054$ compared with 104.0 ± 19.6 kPa, $V_\sigma^{\text{Common suture}} = 0.188$) (Extended Data Fig. 5b).

Intelligent robotic suturing enabled by sliputure

Robotic surgery is known for its high precision, visualization, dexterity and ergonomic benefits[3,27]. However, in existing robotic suturing, the surgeon operates the robot to control the suturing process by observing tissue deformation, which can cause significant inter-individual variation owing to the lack of force feedback[7]. The sliputure proposed here provides an intelligent route to limit suturing force during robotic operations. Once the slipknot is observed to open, a pre-encoded force signal is transmitted to the suture to enable intelligent operation to gauge surgical knot tying during robotic surgery based on visual cues (Fig. 4a). Compared with common suturing with inconsistent tension, sliputure-assisted robotic operations with human-in-the-loop demonstrated high consistency and accuracy (102.0 ± 8.2 kPa, $V_\sigma^{\text{Sliputure}} = 0.080$ compared with 106.8 ± 22.1 kPa, $V_\sigma^{\text{Common suture}} = 0.207$) for multiple surgical knots (Fig. 4b,c, Extended Data Fig. 5d–f and Supplementary Videos 9 and 10). Standing sutures with sliputures produced a flat appearance of the tissue with sufficient blood supply compared with traditional stapled procedures and continuous sutures (Supplementary Fig. 11). The sliputure is also sometimes compatible with continuous sutures (Supplementary Fig. 12), thereby extending its applicability across diverse surgical scenarios. The sliputure is designed to work with the current robotic systems, which are not equipped with dedicated force sensors. We integrated a vision-based automatic-braking module into a customized da Vinci Xi robotic system. This system was re-engineered to ensure seamless sliputure interfacing and uses real-time image processing for slipknot detection. After slipknot release is detected, the system controller immediately issues a stop command to arrest instrument motion, which then effectively prevents suture overpulling. This integrated system was validated in both silicone models and in vivo porcine repairs of colonic injury. The results confirmed its reliable performance through visual force feedback and significantly enhanced the applicability of sliputures in robotic surgery (Fig. 4d,e, Supplementary Fig. 13 and Supplementary Videos 11 and 12). During the suturing process, the robotic arm pulls the slipknot (Fig. 4d), and the corresponding geometric changes (Fig. 4e) are tracked by an image-processing system. When the critical moment of slipknot opening is detected (Fig. 4d,e, far right images), the robotic arm automatically halts to prevent overpulling (Supplementary Video 13). We also incorporated sliputure into collaborative robotic arms for intelligent operation without human intervention (Supplementary Figs. 14 and 15).

Discussion

We developed a mechano-intelligent transmission mechanism based on the slipknot and validated its precision and robustness in delivering force signals for clinical practice and robotic operation (Fig. 4f). This mechanism is particularly well suited for minimally invasive surgery, a representative application for sliputures, in which limited operating space and restricted access to electronic devices present significant challenges[28]. Sliputures overcome these constraints through a mechano-intelligent design that does not require advanced materials or electronics. They offer advantages in simplicity and disposability over conventional force-limiting devices (Supplementary Table 1). Given the substantial cost of electronic force-sensing devices, easily fabricated sliputures are highly economical, functioning without additional cost or equipment. An automatic slipknot fabrication machine enables standardized and on-demand production to support scalable application (Supplementary Fig. 16 and Supplementary Video 14).

Our sliputure strategy is applicable to both open and minimally invasive surgeries, for which limiting the knotting force is critical. Such procedures include those that involve standing sutures in abdominal operations, particularly those performed in confined spaces such as anastomotic reconstruction of narrow luminal structures[29] and surgeries that demand precise knot tension, including corneal repair and vascular suturing[30]. Conventional surgical practices are maintained when using sliputures, and there is no need for additional procedures to limit the knotting force. The strategy is also compatible with robotic systems to provide intelligent operation. Sliputures maintained their functionality even when the slipknot was positioned far from the surgical site, which enables it to avoid areas affected by blood occlusion during suturing. Moreover, the strategy is compatible with continuous sutures (Supplementary Fig. 12), thereby extending its applicability across diverse surgical scenarios. Sliputures can serve not only as training tools but also as practical replacements for conventional surgical sutures, which may be of particular benefit in resource-limited regions with restricted access to medical equipment and training. We also extended this mechano-intelligent strategy in robotic design to enhance safety. By integrating a programmed slipknot into the actuation pathway of a tendon-driven robotic arm (Fig. 4f–h), the system

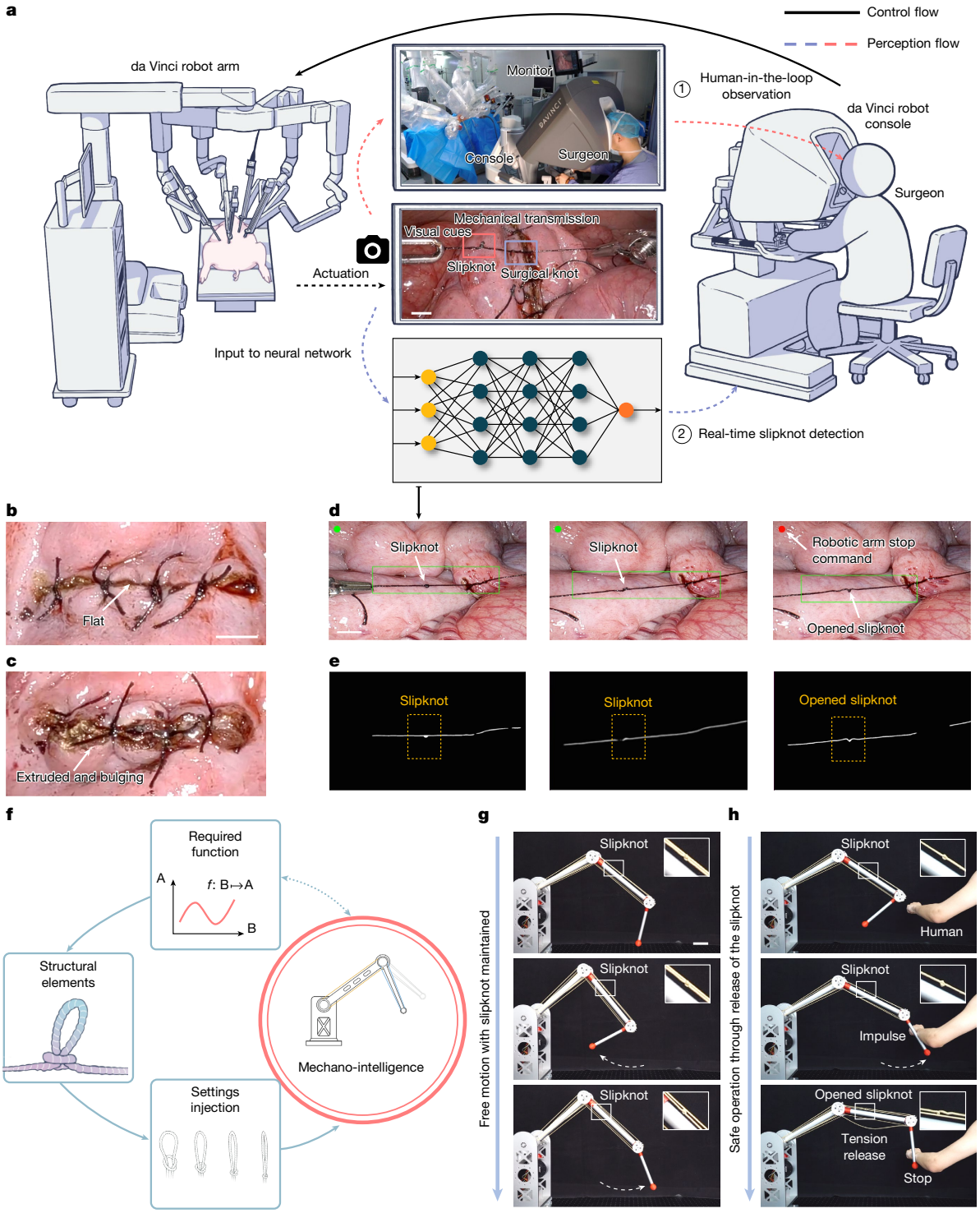

Fig. 4 | A slipknot gauges the intelligent operation of robots. a, The mechanical transmission route of applying sliputures in robotic surgery. Real-time imaging provides visual cues to humans and robots to enable intelligent operation to gauge the surgical knot-tying force. **b**,**c**, Repaired tissue regions of the colon in live pigs by robotic surgery show a flat appearance with sliputures (**b**) but tissue extrusion and bulging with common sutures (**c**). Scale bar, 5 mm. **d**, A closed-loop robotic system that uses sliputures for active arm-movement control was validated through a vision-based automatic-braking experiment in an in vivo porcine model. Real-time image processing for slipknot detection. After the slipknot opens, a stop command was activated to terminate movement of the robotic arm. Scale bar, 5 mm. **e**, The slipknot was detected from the RGB images and converted into real-time greyscale images. Slipknot opening was detected by matching the images to the opened slipknot configuration. **f**, Protocol and methods of slipknot-gauged mechanical transmission. **g**,**h**, Slipknot-enhanced safer human–robot interactions. Scale bar, 5 cm. **g**, The proposed slipknot-integrated tendon-driven robotic arm demonstrates free motion capability at the elbow and wrist joint with the slipknot maintained. **h**, During human–robot interactions, the slipknot is opened and releases the tension when the robot is overloaded by mishandling, which provides a safeguard for the operation.

autonomously interrupts force transmission, acting as a fuse when the tensile load exceeds the F_{peak}. This system can be implemented in various robots to prevent structural overload and to ensure safe operation during human–robot interactions.

The mechano-intelligence exhibited in slipknots may inspire investigations of knotted structures across multiple length scales. The opening of slipknotted DNA molecules showcases how mechanical transmission behaviours can be gauged at the nanoscale (Supplementary Fig. 17 and Supplementary Video 15). Slipknots act as mechano-intelligent mediators in situations in which filaments are used. The mechanical information embedded in other structural elements remains to be discovered, which could expand the mechano-intelligence of this system to broader applications.

Online content

Any methods, additional references, Nature Portfolio reporting summaries, source data, extended data, supplementary information, acknowledgements, peer review information; details of author contributions and competing interests; and statements of data and code availability are available at https://doi.org/10.1038/s41586-025-09673-w.

1. Ashley, C. W. *The Ashley Book of Knots* Vol. 13 (Doubleday, 1944).
2. Sugiyama, T. et al. Forces of tool–tissue interaction to assess surgical skill level. *JAMA Surg.* **153**, 234–242 (2018).
3. Diana, M. & Marescaux, J. Robotic surgery. *Br. J. Surg.* **102**, e15–e28 (2015).
4. Del Dottore, E., Mondini, A., Rowe, N. & Mazzolai, B. A growing soft robot with climbing plant-inspired adaptive behaviors for navigation in unstructured environments. *Sci. Robot.* **9**, eadi5908 (2024).
5. Rothemund, P. et al. Shaping the future of robotics through materials innovation. *Nat. Mater.* **20**, 1582–1587 (2021).
6. De Rooij, T. et al. Laparoscopic pancreatic surgery for benign and malignant disease. *Nat. Rev. Gastroenterol. Hepatol.* **13**, 227–238 (2016).
7. Abiri, A. et al. Tensile strength and failure load of sutures for robotic surgery. *Surg. Endosc.* **31**, 3258–3270 (2017).
8. Adams, C. C. *The Knot Book: An Elementary Introduction to the Mathematical Theory of Knots* (American Mathematical Society, 2004).
9. Grandgeorge, P. et al. Mechanics of two filaments in tight orthogonal contact. *Proc. Natl Acad. Sci. USA* **118**, e2021684118 (2021).
10. Johanns, P. et al. The shapes of physical trefoil knots. *Extreme Mech. Lett.* **43**, 101172 (2021).
11. Grandgeorge, P., Sano, T. G. & Reis, P. M. An elastic rod in frictional contact with a rigid cylinder. *J. Mech. Phys. Solids* **164**, 104885 (2022).
12. Audoly, B., Clauvelin, N. & Neukirch, S. Elastic knots. *Phys. Rev. Lett.* **99**, 164301 (2007).
13. Luo, K., Rothemund, P., Whitesides, G. M. & Suo, Z. Soft kink valves. *J. Mech. Phys. Solids* **131**, 230–239 (2019).
14. O'Reilly, O. M. *Modeling Nonlinear Problems in the Mechanics of Strings and Rods* (Springer, 2017).
15. Melancon, D., Gorissen, B., García-Mora, C. J., Hoberman, C. & Bertoldi, K. Multistable inflatable origami structures at the metre scale. *Nature* **592**, 545–550 (2021).
16. Patil, V. P., Sandt, J. D., Kolle, M. & Dunkel, J. Topological mechanics of knots and tangles. *Science* **367**, 71–75 (2020).
17. Treasure, T. Surgeons' knots: old skills, new training. *Lancet* **359**, 642 (2002).
18. Kirk, R. M. *Basic Surgical Techniques* (Elsevier Health Sciences, 2010).
19. Johanns, P. et al. The strength of surgical knots involves a critical interplay between friction and elastoplasticity. *Sci. Adv.* **9**, eadg8861 (2023).
20. Reischl, S., Wilhelm, D., Friess, H. & Neumann, P.-A. Innovative approaches for induction of gastrointestinal anastomotic healing: an update on experimental and clinical aspects. *Langenbecks Arch. Surg.* **406**, 971–980 (2021).
21. Hammond, J., Lim, S., Wan, Y., Gao, X. & Patkar, A. The burden of gastrointestinal anastomotic leaks: an evaluation of clinical and economic outcomes. *J. Gastrointest. Surg.* **18**, 1176–1185 (2014).
22. Yauw, S., Wever, K., Hoesseini, A., Ritskes-Hoitinga, M. & Van Goor, H. Systematic review of experimental studies on intestinal anastomosis. *Br. J. Surg.* **102**, 726–734 (2015).
23. Ma, Z. et al. Bioinspired tough gel sheath for robust and versatile surface functionalization. *Sci. Adv.* **7**, eabc3012 (2021).
24. Yuk, H. et al. Dry double-sided tape for adhesion of wet tissues and devices. *Nature* **575**, 169–174 (2019).
25. Smit, D. et al. Improving training of laparoscopic tissue manipulation skills using various visual force feedback types. *Surg. Endosc.* **31**, 299–308 (2017).
26. Huang, X. et al. An intelligent grasper to provide real-time force feedback to shorten the learning curve in laparoscopic training. *BMC Med. Educ.* **24**, 161 (2024).
27. Kinross, J. M., Mason, S. E., Mylonas, G. & Darzi, A. Next-generation robotics in gastrointestinal surgery. *Nat. Rev. Gastroenterol. Hepatol.* **17**, 430–440 (2020).
28. Zachariou, Z. *Pediatric Surgery Digest* (Springer, 2022).
29. Brunner, M. et al. Continuous or interrupted suture technique for hepaticojejunostomy? A national survey. *BMC Surg.* **18**, 84 (2018).
30. Lee, W. B. & Mannis, M. J. in *Ophthalmic Microsurgical Suturing Techniques* (ed. Macsai, M. S.) 49–59 (Springer, 2007).

Methods

Fabrication of the slipknot

All experiments were conducted at room temperature (21 °C). The loading rate was set at 10 mm min^{-1} during the slipknot-tying process. To ensure the reproducibility of the slipknots, we used a standardized fabrication method with a 3D-printed string-wrapping board. The designed grooves of the board conformed to the spatial configuration of the slipknot (Extended Data Fig. 1). String was wrapped along these grooves to produce standardized slipknots. The upper right side and lower right end of each slipknot were clamped, and the untightened slipknot was subjected to tension using a Zwick/Roell Z010 testing machine until a preset force F_{tying} was achieved. Following this procedure, standardized slipknots with F_{tying} were fabricated.

High-speed camera recordings

We used a high-speed camera (C321, Phantom) to capture the evolution of slipknot configurations during release from the front view (Fig. 2a(i–v)). The camera operated at 11,000 f.p.s. with a 10-μs electronic shutter speed using macro lenses (100MM F2.8 CA-Dreamer Macro ×2 lenses, Anhui Changgeng Optics Technology). It recorded images at 640 × 128 pixels with a 10-bit depth.

Micro-CT scanning

We used a micro-CT system (Xradia 610 Versa, Zeiss) with a voxel size of 1.3 × 1.3 × 1.3 μm^3 to scan slipknots and to reconstruct their 3D structures based on five typical states. The micro-CT system was set to operate at 120 kV and 17.5 W. Each scan involved an exposure time of 2,500 ms per projection, during which the slipknots were securely positioned and examined for approximately 170 min. We fabricated an in situ tensile fixture (Supplementary Fig. 18) that fit in the sample chamber of the micro-CT scanner. This fixture enabled application of a preset tensile force to the slipknot, allowing it to be gradually opened to any desired state and maintaining it in a stable configuration throughout the scanning process. Micro-CT modelling and analyses were performed using Amira 3D software (v.2021.1, Thermo Fisher Scientific).

FEM of slipknots

FEM of the string slipknot was performed using Abaqus 2020 and the Abaqus/Explicit solver for computations. A model representing the slipknot was formulated using 8-node linear brick mesh elements with reduced integration and hourglass control (C3D8R). The material behaviour of the string was characterized by elastoplasticity. Elasticity was captured by using linear elasticity with an elastic modulus of 2,700 MPa and a Poisson's ratio of 0.49. The plasticity was captured by using a plasticity model of combined hardening by fitting cyclic tensile test data (Supplementary Note 1 and Supplementary Fig. 19). The contact condition was modelled using a general contact-type interaction with a friction coefficient of 0.16 (Extended Data Fig. 6).

The simulation processes of slipknot tying, tightening and opening were visualized. First, the string was tied into a slipknot by implementing prescribed displacement sequences to the key points along the string. Second, the slipknot was tightened with a preset force. The pre-tension was maintained in one step and was unloaded afterwards. Third, the slipknot was opened by moving the free end away from the fixed end.

Mechanical test

We conducted a series of mechanical tests to explore the mechanical characteristics of slipknots, including consistency tests, parametric relationship tests and stability tests. All slipknots were made of fluorocarbon string (YGK) and each test contained five samples.

In the consistency test, 500 slipknots with single-knot loops were fabricated with a string diameter of d = 0.235 mm and a preset force F_{tying} = 7.500 N. In the parametric relationship test, we studied the influence of the number of knot loops, the preset force F_{tying} and the string diameter d on the open force F_{peak}. First, we used string (d = 0.235 mm) to fabricate slipknots with different knot-loop numbers (single, double or triple) and different preset forces of F_{tying} (2.500 N, 5.000 N, 7.500 N, 10.000 N, 12.500 N, 15.000 N and 17.500 N). Next, with F_{tying} = 5.000 N, we used string of different diameters (0.148 mm, 0.165 mm, 0.235 mm, 0.285 mm and 0.333 mm) to fabricate slipknots with different knot-loop numbers (single, double or triple). In the stability test, the slipknots were tested after a time period (day 1, 2, 4, 8, 16, 24 and 32). The tested slipknots had a string diameter of d = 0.235 mm and different knot-loop numbers (single, double or triple). All the slipknot samples were tested using a Zwick/Roell Z010 testing machine. The slipknots were opened at a speed of 50 mm min^{-1}, and the F_{peak} values were recorded. Finally, in the stability test, slipknots (d = 0.235 mm) with different knot-loop numbers (single, double or triple) were opened at different speeds (5 mm min^{-1}, 10 mm min^{-1}, 20 mm min^{-1}, 40 mm min^{-1}, 60 mm min^{-1}, 80 mm min^{-1} and 100 mm min^{-1}), and the F_{peak} values were recorded.

Friction test

We conducted friction tests to measure the kinetic friction coefficients of three types of filaments: fluorocarbon monofilament (d = 0.235 mm, YGK), braided absorbable sutures (4-0 Vicryl, Ethicon) and braided non-absorbable sutures (4-0 Mersilk, Ethicon). Tests were carried out under dry, moist and lubricated conditions. The moist conditions included synthetic blood (Phygene Biotechnology), simulated body fluid (Phygene Biotechnology) and natural saline (Phygene Biotechnology). The lubricated condition was silicone oil 10 mPa·s (Aladdin). We established a friction measurement fixture, whereby a filament was suspended above a spiral tube through a pulley system (Extended Data Fig. 3a). Bearings applied the controllable normal force (F_n) to press the filament firmly against the spiral tube, which was wrapped with the same filament. The spiral tube was placed in a tank to enable tests in moist and lubricated conditions. By steadily pulling the filament using a universal testing machine, the tangential force (F_τ) was measured. F_τ under varying F_n was recorded and analysed through linear regression to determine the kinetic friction coefficient of the filament. The friction coefficients in moist and lubricated conditions were evaluated by dripping different volumes of liquids onto the filament–tube contact region. We also replaced the spiral tube with a silicone block to measure friction coefficients between the filament and silicone (Extended Data Fig. 3b–d).

Opening sliputures under dry, moist and lubricated conditions

To examine whether exposure to fluid in a real surgical environment interacts with the slipknot, which would further influence the F_{peak}, we conducted a series of opening sliputure tests using various types of filaments, including fluorocarbon monofilament (YGK), braided absorbable sutures (Vicryl, Ethicon) and braided non-absorbable sutures (Mersilk, Ethicon) (Extended Data Fig. 4). Each material was tested under dry, moist and lubricated conditions, with five samples per group. For fluorocarbon monofilaments, we used string (d = 0.235 mm) to fabricate slipknots with double-knot loops and different preset forces of F_{tying} (2.500 N, 5.000 N, 7.500 N and 10.000 N). For braided absorbable sutures and non-absorbable sutures, strings (4-0, d = 0.150 mm) were used to fabricate slipknots with double-knot loops and different preset forces of F_{tying} (0.100 N, 0.200 N, 0.350 N, 0.400 N, 0.800 N, 1.600 N and 3.200 N). All the samples were tested using a Zwick/Roell Z020 testing machine in dry conditions, in synthetic blood (Phygene Biotechnology), in simulated body fluid (Phygene Biotechnology), in natural saline (Phygene Biotechnology) and in silicone oil 10 mPa·s (Aladdin). The slipknots were released at a speed of 30 mm min^{-1}, and the F_{peak} values were recorded.

Wearable knot-tying force test platform

A wearable knot-tying force test platform (Supplementary Fig. 20) was constructed to accurately measure the tension in sutures during

a surgical suturing process. The platform consisted of a knob, two pulleys, a slider, a steel wire and a load cell (SBT641C, Simbatouch). One end of the suture was secured to the slider through the knob, and the adjacent pulley guided the suture, thereby minimizing the impact of hand-posture variations on force measurement. The slider was connected to the load cell by a steel wire (d = 0.8 mm) running through the upper pulley. During suturing, the surgeon positioned their index finger through a hole in the device, with the thumb resting on the shell above the pulley next to the load cell. Tension in the suture was directly measured by the load cell as the suture was pulled through the platform.

Bimanual real-time dynamometer

A bimanual real-time dynamometer platform was developed to accurately capture tensile forces applied by both hands during surgical knot tying. The system consisted of a medical sterile interface, a passive revolute joint and a quick connector (Supplementary Fig. 21a). The sterile interface ensured clinical compatibility, and the passive revolute joint provided a free rotational range of 80° (Supplementary Fig. 21b), which enabled natural wrist movement and reduced the influence of hand posture or angle on measurements. To eliminate angular interference and to achieve high-fidelity force data, the dynamometer adopted a decoupled mechanical structure (Supplementary Fig. 21c), and the force applied through the suture was transmitted directly through the joint to the internal sensor. Notably, the platform supports simultaneous use of two devices, one for each hand, which enabled real-time, bilateral force measurement.

Knot-tying force test across surgeons

To assess the clinical feasibility of the sliputure transmitting force, we designed a knotting-force test platform to measure knotting-force precision and incision pressure (Supplementary Fig. 4). This platform comprises three major components: (1) the desired sliputure with a slipknot on a braided common suture (4-0 Mersilk, Ethicon); (2) a silicone practice model with pressure-sensitive films (4LW, Fuji film Prescale); and (3) a real-time dynamometer. Fabricating the sliputure with an F_{peak} of 1.400 N (F_{tying} = 0.350 N), we evaluated the impact of sliputure transmitting force on the knotting-force performance of surgeons[31,32]. Ten junior surgeons and five senior surgeons were randomly selected and recruited for the experiment. Junior surgeons were defined as surgeons with fewer than 10 years of clinical experience, whereas senior surgeons were those with more than 10 years of clinical experience. Each surgeon performed knot tying (n = 20) with common sutures (n = 10) and sliputures (n = 10). The real-time dynamometer collected data on the force used, and then we acquired the force data after data transformation (Supplementary Figs. 3a and 4). All force data were used for further comparative analyses.

Incision pressure test of standing sutures

To evaluate the mechanical transmission ability of the sliputure, we used a silicone practice model along with pressure-sensitive film (4LW, Fuji film Prescale) to quantify incision pressures of standing sutures using sliputures and common sutures (Supplementary Fig. 3b). In the silicone practice model, we performed a 7-cm incision by laser cutting to simulate a wound. Adjacent to the incision at 0.5 cm from either side, 2 sets of circular holes measuring 1 mm in diameter were introduced parallel to the trajectory of the incision. These circular holes facilitated the entry and exit of the needle during the suturing process. To eliminate any interference among needles, a longitudinal spacing of 1 cm was maintained between neighbouring circular holes. Leveraging the midpoint of the feasible force range, we prepared an engineered slipknot (4-0 Mersilk, Ethicon) with an F_{peak} value of 1.300 N for subsequent experiments. Pressure-sensitive films (film A for colour rendering and film B for pressure assessment) were precisely positioned to match the contour of the simulated wound. Following the process of suturing and pre-tying knots, the pressure exerted by the slipknot on both sides of the wound made a red colour in film B. To ensure consistency, senior surgeons performed the same suturing procedures using both sliputures (n = 25) and common sutures (n = 25) on the silicone practice board. These suturing trials were conducted under open, laparoscopic (Hefei DVL Electron) and robotic (Intuitive Surgical-Fosun Medical Technology) surgical settings. During robotic surgery, the knotting velocity of the surgeon was quantified using Tracker (v.6.0.9). Subsequently, the colour intensity of the pressure-sensitive film A, which corresponded to the applied pressure, was quantified by scanning the images and converting them into numerical values using commercial software (Fuji film FPD8010E v.2.5.0.3).

Incision pressure test of continuous sutures

To evaluate the stress distribution of continuous sutures, we performed incision pressure tests of continuous sutures[33] (n = 5) of five stitches on a silicone practice model (Extended Data Fig. 7 and Supplementary Note 4). After excluding the influence of the anchor knot (first stitch) and the final knot (last stitch) on incision pressure, we chose the middle three stitches based on the oblique trajectory of the suture in continuous sutures. Subsequently, the pressure-sensitive films (4LW, Fuji film Prescale) embedded in the silicone were removed, and the films corresponding to the middle three stitches were selected for analyses. Colour changes were quantified by scanning the images and converting them into numerical values using commercial software (Fuji film FPD8010E).

Bimanual knot-tying force test

The bimanual knot-tying force test was conducted to measure and compare the forces on both sides of the sliputures (Supplementary Fig. 22). Five junior surgeons and five senior surgeons were randomly recruited for the experiment. Each surgeon wore real-time dynamometers bimanually and performed knot tying using sliputures of double-knot loops (4-0 Mersilk, Ethicon) with an F_{peak} value of 1.300 N (n = 10). During the test, the side with the slipknot was pulled and the peak force was defined as T_{active}, whereas the other side without the slipknot was held stationary and the peak force was referred to as T_{fixed}. The process was stopped after the release of the slipknot. The F_{peak} values from both dynamometers were recorded for comparison.

The buffer zone of sliputures

The buffer zone of sliputures was determined through uniaxial tensile testing. Specifically, sliputures of double-knot loops (4-0 Mersilk, Ethicon) with an F_{peak} value of 1.300 N were used. Tests were conducted using a Zwick/Roell Z020 testing machine, equipped with an Xforce HP load cell (capacity of 200 N). Under uniaxial tensile loading of 10 mm min^{-1}, the sliputures released and then formed a buffer zone after relaxation, where the suture remained kinked and bore zero load (Extended Data Fig. 8).

Sliputures for continuous sutures

The sliputures used for continuous suture of five stitches was as follows. At the first stitch, we used a sliputure (Suture A, 4-0 Vicryl, Ethicon) to tie an anchor knot at the proximal end of the incision. Continuous sutures of four stitches were then performed using the same suture procedure as usual, leaving the final stitch unknotted. Subsequently, a second sliputure with two slipknots (Suture B, 4-0 Mersilk, Ethicon) was used to place one stitch at the distal end of the incision, with the slipknot near the incision being first used to form an anchor knot. Finally, two sutures were tied together to complete the final knot (Supplementary Fig. 12).

Feasible force-range exploration

To systematically explore the feasible force range for colonic injury repair, a mechanical test platform was assembled (Supplementary Fig. 5a,b). This platform included the specimens to be tested, a dedicated tensiometer (DS2-50N, Zhiqu), a digitally controlled electric machine, a pump, a manometer and PBS solution containing methylene blue.

The experimental procedure (Supplementary Fig. 5c) involved the introduction of a 2-mm-diameter injury into an ex vivo rat colon, specifically those of Sprague–Dawley rats weighing between 200 and 250 g ($n = 20$). The injury was generated using a biopsy punch (Dynarex). Subsequently, the punctured colon was bathed in a continuous solution of methylene blue maintained at a pressure of 20 mmHg. Pre-suturing was carried out using common sutures (4-0 Mersilk, Ethicon). During the experimental phase, one end of the common suture remained secured, whereas the other end was horizontally pulled by the tensiometer at a controlled rate of 10 mm min^{-1}. The tension applied was consistently monitored in real-time throughout the process. Post-test analyses involved categorizing the tension as F_{min} once the injury was successfully repaired without leakage. Conversely, the tension was labelled as F_{max} when the colonic wall tore and leakage occurred. The boundaries of the feasible force range were subsequently determined based on the F_{min} and F_{max} values. The feasible force range can also be predicted by mechanical modelling (Supplementary Note 5).

Ex vivo and in vivo rat colonic injury repair

To compare the sliputure transmitting force in both ex vivo and in vivo conditions, we conducted experiments using female Sprague–Dawley rats weighing between 200 and 250 g. The rats were randomly divided into two groups: the ex vivo group ($n = 5$) and the in vivo group ($n = 5$). The experiments involving the sliputure (target $F_{peak} = 1.300$ N) were carried out on an automated mechanical test platform (Supplementary Fig. 5a,b). For both ex vivo and in vivo tests, a 2-mm-diameter injury was introduced to the resected colon using a biopsy punch (Dynarex). Subsequently, the injury was repaired by the tensiometer at a consistent rate of 10 mm min^{-1} using a sliputure under 20 mmHg of intraluminal pressure. After the availability of the opened signal of the slipknot, we recorded the force data from the tensiometer and halted the electric machine to stop the tensiometer. Afterwards, a reverse knot was tied to secure the surgical knots (surgeon's knot). For the in vivo test, the distal colon and small intestine were clamped 2-cm apart from the repaired region. PBS solution containing methylene blue was introduced through the repair area to assess colonic leakage. In summary, we compared the force data and operation efficacy of colonic leakage between ex vivo and in vivo groups to evaluate the mechanical transmission of sliputures.

Comparison of anastomotic leakage, postsurgical adhesion and tissue ischaemia

Female Sprague–Dawley rats weighing between 200 and 250 g were randomly allocated into two groups: the sliputure group and the common suture group. This division aimed to facilitate a comparative study of anastomotic leakage, postsurgical adhesion and tissue ischaemia. The experimental procedures were performed by a junior surgeon with 2 years of clinical experience. This surgeon was affiliated with the Department of General Surgery of another tertiary hospital and had no conflict of interest. To minimize bias, the surgeon was blinded to the study objectives while tying the common sutures. Following a 24-h fasting period, rats were anaesthetized through intraperitoneal administration of ketamine (80 mg kg^{-1}). The rats were then placed on a heated pad for the surgery. After abdominal hair was removed, laparotomy was performed to expose the colon. Using a biopsy punch (Dynarex), a 2-mm-diameter injury was created in the colon. In the subgroup focusing on leakage, the injury was repaired using sliputures ($n = 10$) with an F_{peak} value of 1.300 N, whereas common sutures were used in the control group ($n = 10$). To observe and compare colonic leakage, the distal colon and small intestine were clamped 2 cm away from the repaired region. Subsequently, PBS solution containing methylene blue was injected through the repair site. In the subgroup assessing adhesion, after colonic injury repair as described above, continuous sutures (4-0 Mersilk, Ethicon) were used to close the peritoneum, and interrupted sutures (4-0 Mersilk, Ethicon) were used to close the abdomen. On the seventh day postoperatively, the repaired colon was exposed and adhesion rates were observed and compared between the sliputure-treated group ($n = 10$) and the common-suture-treated group ($n = 10$). In the subgroup assessing tissue ischaemia, visualization of vascular conditions before and after biopsy puncture, as well as after repair using sliputures or common sutures, were carried out. This visualization was accomplished by LSCI. The same procedures for colonic injury repair and abdomen closure were performed. After concluding of all tests, the rats were humanely euthanized by CO_2 inhalation.

Comparison of wound healing

Female Sprague–Dawley rats weighing between 200 and 250 g were randomly allocated into two groups: the sliputure group and the common suture group. In each group, subgroups were divided as sliputure D1–D8 and common suture D1–D8 based on postsurgical days. The entire experimental process was carried out in a sterile environment. The preoperative preparations were consistent with the procedures outlined above. Through laparotomy, the colon of the rat was exposed, and a 2-mm-diameter injury was introduced using a biopsy punch (Dynarex). Sliputures and common sutures were used to repair the injury in the sliputure group and the common suture group, respectively. Postoperative assessments spanned from day 1 to day 8, which included animal euthanasia under CO_2 inhalation, daily tissue collection and burst pressure measurement in both groups ($n = 3$). On postoperative day 5, blood collection and analyses were conducted on a subset of rats in both the sliputure and common suture groups before humane euthanasia using CO_2 inhalation. The regions after repair were excised, fixed in 10% formalin for 24 h and prepared for histological analyses.

LSCI

Vessel visualization of the targeted colon area was conducted before and after biopsy puncture, as well as following the repair procedures using sliputures or common sutures, using LSCI. To mitigate potential motion artefacts, the targeted colon region was gently externalized and positioned on gauzes for stabilization. The maintenance of a stable blood flow was achieved through the continuous use of 37 °C saline solution. Once the parameters were set, HD mode was used to capture a clear speckle image depicting the distribution of blood flow in the intact target region of the colon. The exposure time for image acquisition was set at 5 s. Subsequently, after the introduction of a 2-mm-diameter biopsy puncture, additional speckle images were obtained using LSCI under the same parameter settings and measurement time. Following this, surgeons proceeded to repair the colonic injury with both sliputures and common sutures, and LSCI was used to capture speckle images with the same parameter settings and measurement time. This imaging process aimed to track and visualize the vascular dynamics of the targeted colon region before, during and after the surgical interventions to provide insights into the effects of the repair methods on blood flow and tissue perfusion. The data were collected using a Laser Speckle Contrast Imaging system RFLSI III (v.4.0).

H&E and multiplex immunofluorescence staining

Tissue samples were collected from rats at designated time points and fixed with 4% paraformaldehyde. Next, 4-μm-thick slides were cut from the paraffin-embedded intestinal tissue. For H&E staining, the slides were deparaffinized and rehydrated through graded alcohol solutions to water and stained with H&E for nucleus and cytoplasm staining. After dehydration, the stained slides were placed in mounting medium. Multiplex immunofluorescence staining was performed according to the manufacturer's instructions using a multiplex fluorescence immunohistochemical staining kit (Genecast Biotechnology). In brief, 4-μm-thick slides were deparaffinized, rehydrated and boiled in epitope retrieval solution for 15 min. After cooling to room temperature, antibody block solution was used to block endogenous peroxidase for 10 min at room temperature. Primary antibody incubation, secondary

antibody incubation and tyramine signalling amplification visualization were the procedures used to label one antigen. CD86 (19589S, CST, 1:400) and CD206 (60143-1-ig, Proteintech, 1:5000) were sequentially stained. The slides were placed in antifade mounting medium. Images were taken using a slide scanner (Hamamatsu, Nano Zoomer S60) and fluorescence microscopy (Nikon, Eclipse C1). Image data were collected using CaseViewer software (v.2.4).

Laparoscopic application of sliputures in a live porcine model

In vivo porcine experiments used female Bama miniature pigs (23–27 kg, 5–6 months of age) to demonstrate the application and function of the slipknot in laparoscopic surgery. The laparoscopic platform (Fig. 3j) was acquired from Karl Storz. After fasting for 24 h, pigs were premedicated with intramuscular atropine (0.04 mg kg^{-1}), ketamine (10 mg kg^{-1}) and midazolam (0.6 mg kg^{-1}), induced with isoflurane (4%), endotracheally intubated and maintained with isoflurane (1–2%) during surgery. We placed the pigs in dorsal recumbency and aseptically prepared the abdominal region. Several trocars (Endopath Xcel, Ethicon and Kangji Medical) were placed on the abdomen to enable access of surgical instruments and a camera. Surgeons identified the colon and made a 1-cm-wide incision in the colon wall. After cleaning the lumen and disinfecting the intestinal incision, the intestinal injury was repaired using sliputures with inverting interrupted sutures (4-0 Mersilk, Ethicon). A control group in which the injury in the colon wall was repaired using common sutures with inverting interrupted sutures (4-0 Mersilk, Ethicon) was also performed for comparison. Observations for intestinal leakage were made 10 min after the process. The abdominal wall was closed in a multilayer fashion, and the animal was euthanized after the experiment.

Robotic application of sliputures in a live porcine model

In vivo porcine experiments used female Bama miniature pigs (23–27 kg, 5–6 months of age) to demonstrate the application and function of the slipknot in robotic surgery. The robotic platform (Fig. 4a) was acquired from Intuitive Surgical-Fosun Medical Technology. After fasting for 24 h, pigs were premedicated with intramuscular atropine (0.04 mg kg^{-1}), ketamine (10 mg kg^{-1}) and midazolam (0.6 mg kg^{-1}), induced with isoflurane (4%), endotracheally intubated and maintained with isoflurane (1–2%) during surgery. We placed the pigs in dorsal recumbency and aseptically prepared the abdominal region. Several trocars were placed on the abdomen to enable access of surgical instruments and a camera, and one additional trocar (Endopath Xcel, Ethicon) was placed to facilitate assistant operation. Surgeons identified the colon and made a 1-cm-wide incision in the colon wall. After cleaning the lumen and disinfecting the intestinal incision, the intestinal injury was repaired using sliputures with inverting interrupted sutures (4-0 Mersilk, Ethicon). The control group underwent the same procedure, but the repair was made using common sutures. Observation for intestinal leakage were performed 10 min after the process. The abdominal wall was closed in a multilayer fashion, and the animal was euthanized after the experiment.

We performed additional live porcine experiments, including induction of acute colonic perforation with peritonitis and colonic injury repair of female Bama miniature pigs (23–27 kg, 5–6 months of age) to compare the effects of standing sutures using sliputures, staples and continuous sutures under a robotic platform (Intuitive Surgical-Fosun Medical Technology). After fasting for 24 h, pigs were anaesthetized following the same protocol as described above. We placed the pigs in dorsal recumbency and aseptically prepared the abdominal region. Several trocars were placed on the abdomen to enable access of surgical instruments and a camera. Surgeons identified the colon and made three 1-cm-wide incisions in the colon wall at intervals of 3 cm. The abdominal wall was closed in a multilayer fashion.

After fasting for 24 h, the porcine models of acute colonic perforation with peritonitis were anaesthetized following the same protocol as described above, and trocars were inserted at the same incision sites, with one additional trocar (Endopath Xcel, Ethicon) placed to facilitate assistant operation. Surgeons identified the colonic injury, disinfected the intestinal incisions and repaired them using continuous sutures, staples or standing sutures with sliputures. The appearance of tissue as the repaired injury site was recorded. Subsequently, indocyanine green (0.1 mg kg^{-1}) was intravenously administered, followed by a 5 ml saline flush. Under fluorescence imaging of the robotic system, colonic vascular perfusion was observed 60 s after injection. Finally, the abdominal cavity was irrigated with saline and the abdominal wall was closed in a multilayer fashion.

Development and validation of a vision-based sliputure and slipknot detection system

We used the da Vinci Xi robotic system enhanced by a purely vision-based sliputure and slipknot detection system to validate the practicality and applicability of our proposed sliputure as a surgical consumable and non-electronic haptic sensor. To model sliputure and slipknot detection, we formulated it as a regression modelling problem by decoupling this process into sliputure line extraction and opened slipknot detection given by the following equations: Lines = Extractor (I) and Open slipknot = Detector(Lines), where I denotes RGB images of the first-person view from the da Vinci Xi endoscope, and Lines denote a set of sliputure lines extracted by the function Extractor(·). The extracted sliputures Lines were then input into a slipknot detector function Detector(·), which predicts whether there is an opened slipknot. Notably, the reason why we decoupled the modelling process into two parts is to fully leverage the advantages of data-driven methods by converting a specific medical problem into a general modelling problem while ensuring real-time performance for the surgical robotic system under limited data and instrument resources.

Specifically, for sliputure line extraction, we designed an encoder–decoder neural network based on a U-Net[34] structure (named SlipknotNet, shown in Fig. 4a and Extended Data Fig. 9) to model the function Extractor(·), in which the image encoder is realized by a pretrained ResNet50 (ref. 35) and the decoder contains up-convolution operators, SENet[36] modules and a suture-detection module. During the training stage, the parameters of the encoder were frozen using pretrained parameters from ImageNet[37], whereas the parameters of the decoder were trained on over 1,800 annotated images by volunteer surgeons using our custom-made annotation software. We used a joint loss function including dice loss[38] and focal loss[39] using the following equation: Loss = $\alpha \times$ dice loss + $(1 - \alpha) \times$ focal loss. For the open slipknot detection, the function Detector(·) was realized by implementing template matching using the scale-invariant feature transform operator from OpenCV. The entire process of sliputure extraction and slipknot detection is visualized in Fig. 4a.

In both silicone practice models and live porcine colonic injury repair using sliputures teleoperated by the da Vinci Xi robotic system under real-time monitoring in 30 Hz with a local workstation (Ubuntu 22.04, Intel Core i9-14900, NVIDIA RTX 4090m), the aforementioned sliputure and slipknot detection scheme ran with a circle mark. A green mark flashing means no open slipknot detected, which allows continued control of the robotic arm. A red mark means the slipknot is open, and a stop control signal is sent to the robot console by UART communication, and a high-level internal stop from the robot is triggered. Our engineering code and dataset are both open-source and available on our project website[40].

Automated system for standardized and rapid mass production of sliputures

The automated sliputure construction system comprises modules for wire feeding, force control, wire wrapping, slipknot collection and a user interface (Supplementary Fig. 16). The wire-feeding module supplies filament material (diameter of 0.1–2 mm, unlimited length) from a

spool into wire-wrapping module, where it is precisely cut to the desired length. The wire-wrapping module uses coordinated motor-driven and pneumatic actuators to form slipknot configurations with the desired number of knot loops. The force control module, integrated with piezoelectric sensors and precision screw actuators, applies and maintains a F_{tying} (0.1–20 N) on the constructed slipknot. After setting up the parameters, the system operates autonomously without manual intervention, thereby ensuring standardized and rapid mass production of sliputures.

Vision-based robotic dual-arm suture system for the slipknot application

The vision-based robotic dual-arm suture system consisted of two Franka Emika Panda 7 degree-of-freedom arms and a camera. The overall framework of the vision-based dual-arm suture system is illustrated in Supplementary Fig. 14. The reference velocity of the active arm was set as 0.5 cm s^{-1}. Through the real-time processing of greyscale images, the active arm automatically stops based on the opened signal of the slipknot (Supplementary Fig. 15).

DNA slipknot molecular dynamic simulation

Coarse-grained molecular dynamic simulations were performed using the program Gromacs with the Martini 2 force field for nucleic acids. The initial straight DNA structure with randomly assigned sequences had a length of approximately 670 nm and a diameter of 2.2 nm, comprising 130,000 atoms and 28,000 beads. A DNA knot was artificially constructed in the middle of the straight DNA. A triclinic simulation box with periodic boundaries in all three directions was used (Supplementary Fig. 17).

The atomic potential energy was minimized first using 1,000 static steps. In the dynamic simulations, we used a time step of 10 fs. The pressure was maintained at 1 bar with the Nosé–Hoover Langevin piston and the temperature was maintained at 273 K using a Langevin thermostat. The DNA knot was untangled by pulling one end of the DNA at a velocity of 0.01 nm ps^{-1}. The total simulation time for untangling the DNA knot was around 5 ns. The atomic structure was visualized using visual molecular dynamics.

Slipknot-enhanced safe human–robot interactions

Building on the demonstrated clinical success and the inherent capability of slipknots to precisely limit force release, we extended its versatility to robotics by integrating sliputures into a custom-built 4 degree-of-freedom cable-driven robotic arm, engineered as an adjustable mechanical fuse to ensure safe human–robot interactions (Fig. 4g,h, Extended Data Fig. 10 and Supplementary Video 16). The actuation architecture incorporated two direct-drive systems for the base and the shoulder, as well as two independent tendon routes that drive the bidirectional motion of the elbow and wrist joints, with a slipknot strategically embedded in the forearm segment to monitor and regulate inter-joint forces. The actuation transmission pathway is instantaneously interrupted when the tension force at the sliputure exceeds a pre-programmed threshold F_{peak} due to an overloaded external interaction, achieved through slipknot-mediated cable elongation that dissipates stored mechanical energy. This enables simultaneous protection of humans and delicate objects from excessive force and the safeguarding of robotic components from structural overload during impact events. It is worth noting that the capability to flexibly adjust the F_{peak} of the slipknot enables on-demand control of contact loads, a critical feature for human–robot interactions. Unlike traditional solutions, this purely mechanical safety solution operates without requiring auxiliary electronics or additional mass at the end-effector, demonstrating its applicability for seamless integration into existing robotic platforms.

Statistical analysis

Categorical variables were described using frequency and percentage, which were assessed using Fisher's exact tests or Chi-square tests between groups. Continuous variables are presented as the mean and standard deviations, which were compared using Wilcoxon rank-sum tests or Student's *t*-tests. GraphPad Prism (v.9.5.0, GraphPad Software) was used for all statistical analyses in the study. In statistical analyses, the significance thresholds were considered as $^{*}P < 0.05$, $^{**}P \leq 0.01$ and $^{***}P \leq 0.001$.

Animal studies

Study design. No formal sample size calculation was performed, and the number of samples was determined by the maximum available resources. In animal experiments that explored the feasible force range, a sample size of $n = 20$ was used. For ex vivo and in vivo rat colonic injury repair, the sample sizes were $n = 5$ for ex vivo and $n = 5$ for in vivo experiments. For comparison of anastomotic complications, the sample sizes were $n = 10$ in the sliputure group and $n = 10$ in the control group. For comparison of wound healing, the sample sizes were $n = 3$ for each subgroup from days 1–8 in both the sliputure and control groups. Laparoscopic and robotic experiments were conducted with a minimum of one pig per group. No statistical methods were applied to calculate sample sizes. The animal samples prepared by the same method were randomly allocated to each group. Blinding was not used in this study.

Animals. The following animals were used in experiments: female, specific pathogen-free Sprague–Dawley rats aged 4 weeks and weighing 200–250 g; and female Bama miniature pigs aged 5–6 months and weighing 23–27 kg.

Ethics. All animal studies were approved by the Institutional Animal Care and Use Committee at Zhejiang University (ZJU20230084 and ZJU20250067), and postoperative care was supervised at the Animal Experimental Center of Sir Run-Run Shaw Hospital, Zhejiang University.

Surgeon participant studies

Informed consent was obtained from all participants, and the study was approved by the Institutional Review Board of Sir Run Run Shaw Hospital, Zhejiang University (approval numbers 2023-0528 and 2025-0023).

Reporting summary

Further information on research design is available in the Nature Portfolio Reporting Summary linked to this article.

Data availability

All data supporting the findings of this study are provided in the paper, the Extended Data figures and the Supplementary Information. Source data underlying the figures are available from GitHub (https://github.com/Slipknot-Gauged/Source-Data). Source data are provided with this paper.

Code availability

The custom codes used in this study are publicly accessible at GitHub (https://github.com/Slipknot-Gauged/Codelist).

31. Fischer, L. et al. Variability of surgical knot tying techniques: do we need to standardize?. *Langenbecks Arch. Surg.* **395**, 445–450 (2010).
32. Ching, S. S., Mok, C. W., Koh, Y. X., Tan, S.-M. & Tan, Y. K. Assessment of surgical trainees' quality of knot-tying. *J. Surg. Educ.* **70**, 48–54 (2013).
33. Jain, S. K., Stoker, D. L. & Tanwar, R. *Basic Surgical Skills and Techniques* (JP Medical, 2018).
34. Ronneberger, O., Fischer, P. & Brox, T. U-net: Convolutional networks for biomedical image segmentation. In *Proc. International Conference on Medical Image Computing and Computer-Assisted Intervention* (eds Navab, N. et al.) 234–241 (Springer, 2015).
35. He, K., Zhang, X., Ren, S. & Sun, J. Deep residual learning for image recognition. In *Proc. IEEE Conference on Computer Vision and Pattern Recognition*, 770–778 (IEEE, 2016).
36. Hu, J., Shen, L. & Sun, G. Squeeze-and-excitation networks. In *Proc. IEEE Conference on Computer Vision Pattern Recognition*, 7132–7141 (IEEE, 2018).

37. Deng, J. et al. ImageNet: a large-scale hierarchical image database. In *Proc. IEEE Conference on Computer Vision Pattern Recognition*, 248–255 (IEEE, 2009).
38. Li, X. et al. Dice loss for data-imbalanced NLP tasks. In *Proc. 58th Annual Meeting of the Association for Computational Linguistics* (eds Jurafsky, D. et al.) 465–476 (Association for Computational Linguistics, 2020).
39. Lin, T.-Y., Goyal, P., Girshick, R., He, K. & Dollár, P. Focal loss for dense object detection. In *Proc. IEEE International Conference on Computer Vision*, 2980–2988 (IEEE, 2017).
40. Xue, Y. et al. SlipknotNet. *GitHub* https://github.com/Slipknot-Gauged/Codelist (2025).

Acknowledgements We acknowledge the support of the following: the 'Pioneer' R&D Program of Zhejiang (2023C03007), the National Natural Science Foundation of China (T2125009, 12102388, T2293722, 92048302 and 12321002), the National Postdoctoral Program for Innovative Talents (BX20220272), the Key Research and Development Project of Zhejiang Province (2022C01022), the Laoshan Laboratory (LSKJ202205300), the Key Research and Development Project of Zhejiang Province (2021C03061), the Central Government Guided the Local Science and Technology Development Fund Project (2023ZY1040), and the Zhejiang Provincial Natural Science Foundation of China (LR25H160001). We thank Y. Ma for micro-CT scanning and analyses; C. Xing for micro-CT analyses; surgeons from the Department of General Surgery, Sir Run-Run Shaw Hospital for their participation in the study; Z. Chen for his assistance in animal experiments; J. Liang for his technical support with the fabrication and manufacturing of the tendon-driven robotic arm; and D. Du for providing equipment and guidance in the work related to pressure-sensitive films. The laparoscopic and robotic platforms are supported by Hefei DVL Electron, Karl Storz and Intuitive Surgical-Fosun Medical Technology.

Author contributions T.L., X.Y., Y.X., J.C. and W.Y conceived the idea. J.C., Y.X., T.F. and K.Z. developed the methods and fabrication for the slipknot-gauged transmission and sliputures. T.F., S.X., Y.X. and Q.Z. formulated the theoretical model. K.Z., T.F. and Y.X. developed the FEM. Y.X., J.C., K.Z., Jinming Zhang, Zhe Wang, T.F., Z.M. and X.Y. carried out the mechanical tests. Q.H., K.Z. and H.Z. performed coarse-grained molecular dynamic simulations for DNA knots. Y.X., J.C., Y.F., H.G. and H.D. designed and conducted the vision-based robotic test. T.L., Y.X. and H.L. designed the robotic micro-operation experiment, and H.L. and S. Liu. conducted the experiments. T.L., Y.X., Z.C. and Junhui Zhang carried out the experiment of heavy-duty operation. S. Li and Y.X. conducted the high-speed camera recordings. Y.X., K.Z. and L.W. carried out micro-CT scanning. J.C., Y.X., J.H. and S.P. designed and conducted the in vivo and ex vivo animal experiments and histological assessments. J.C., Y.X., H.G. and T.F designed and conducted the knot-tying force test across surgeons. J.C., Y.X. and T.F. carried out the incision pressure test on a silicone model. J.C., Y.X., J.S., T.F. and M.C. carried out the laparoscopic application of sliputures. J.C., Y.X., T.F. and M.C. performed the robotic application of sliputures. T.F., K.Z., J.C., Y.X., Q.Z. and Y.C. collected and analysed the data. F.Z., X.L., J.-W.W., D.R., L.G., X.W. and B.Z. contributed to the mechanical design in this work. J.C., Y.X., T.F., K.Z., H.Z., T.L., S. Li, S.X., X.Y., T.-W.W. and W.Y. wrote the manuscript with input from all authors. The study was supervised by T.L., M.C., X.Y., X.C. and W.Y. During the revision process, the authors contributed as follows: Y.X., J.C., T.F., K.Z., H.G., X.Y., T.L. and W.Y. proposed the overall revision plan of the manuscript. Y.X., W.Z., J.C., X.L. and Zhuofan Wang designed and fabricated the automatic slipknot fabrication machine. H.G., Y.X., J.C. and Jinming Zhang optimized and fabricated the wearable force-measuring system and conducted the related experiments. H.G., Y.X. and X.L. designed and built the tendon-driven robotic arm integrated with sliputures and completed the related experiments. Y.X., Zhe Wang and Zhuofan Wang designed and fabricated a fixture for measuring friction coefficients of sutures in a liquid environment. Y.X. conducted the measurements, and T.F., and E.C. performed data analyses. X.L., T.C. and Y.X. designed and manufactured the uniaxial tensile fixture in a liquid environment. J.C., Zhuofan Wang and Jinming Zhang carried out experiments, and T.F. conducted data analyses. X.Y. designed the cohesion measurement method. T.F. revised the sliputure models considering multi-filament structure, friction and liquid immersion. T.F. and X.Y. developed the predictive model for the feasible range of tissue suturing force. K.Z. investigated the influence of plasticity on the finite element modelling of sliputures. Jinming Zhang, Zhuofan Wang and J.C. prepared various sliputure samples required for the experiments. J.C. developed the application of sliputures in continuous sutures, J.C. and Y.X. carried out the experiments, and T.F. performed data analyses and mechanical modelling. J.C., Y.X., Y.S., X.C. and T.L. designed the experimental setup for sliputure applications using the da Vinci Xi surgical robot, and J.C., Y.X., Y.S., E.Z., Jinming Zhang, J.S., S. Li, Z.M. and Zhuofan Wang conducted experiments and analysed the data. Y.S. developed the image recognition algorithm for sliputures. Y.X., J.C., Jinming Zhang, E.Z., S. Li and B.Z. performed data annotation. Y.X., J.C., T.F., K.Z., S. Li, Y.S., X.Y., T.L. and W.Y. revised the manuscript with input from all authors. Revisions were supervised by T.L., X.Y. and W.Y.

Competing interests The authors declare no competing interests.

Additional information

Supplementary information The online version contains supplementary material available at https://doi.org/10.1038/s41586-025-09673-w.

Correspondence and requests for materials should be addressed to Tiefeng Li, Mingyu Chen, Xuxu Yang, Wei Yang or Xiujun Cai.

Peer review information *Nature* thanks the anonymous reviewers for their contribution to the peer review of this work. Peer reviewer reports are available.

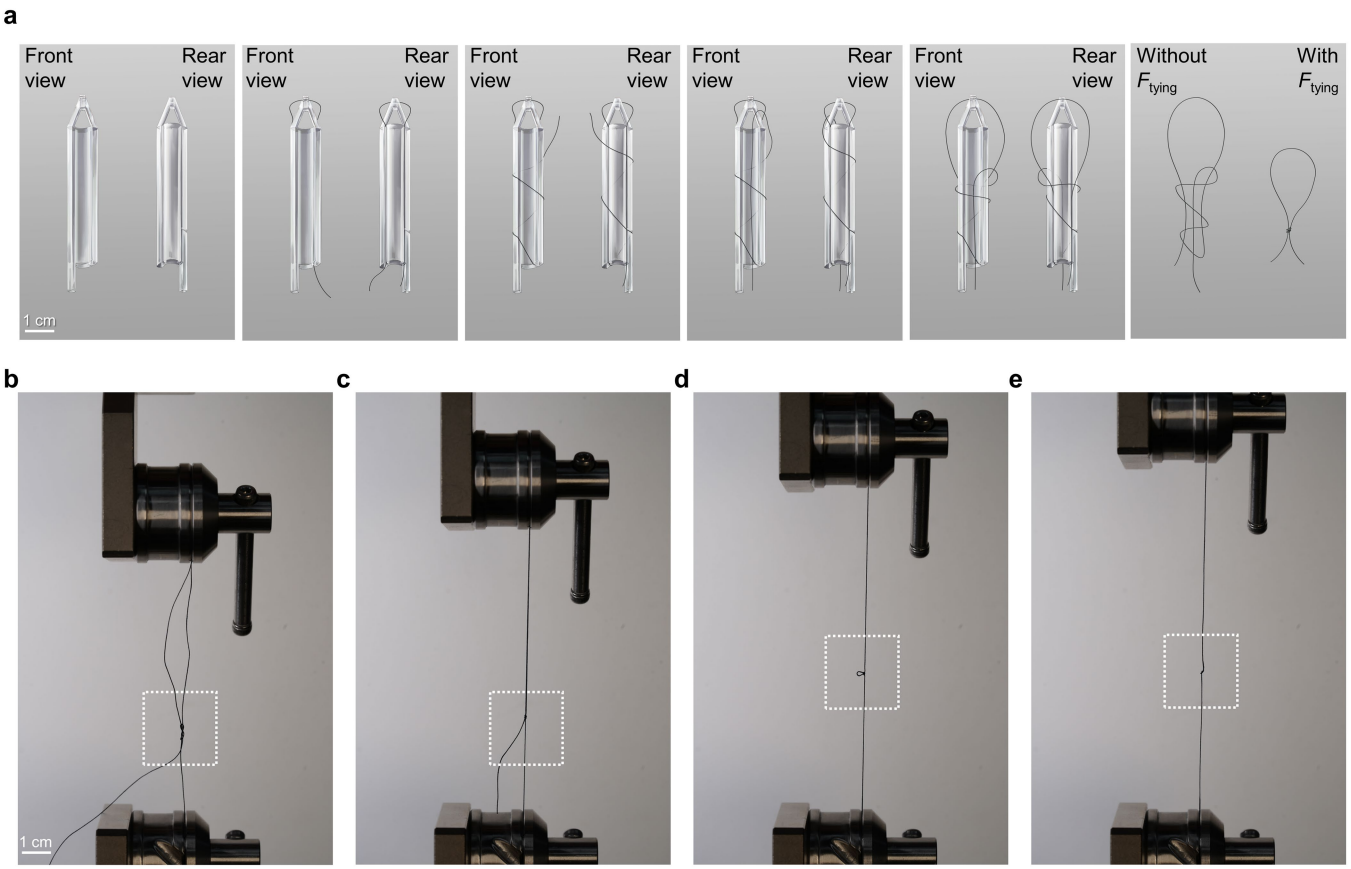

Extended Data Fig. 1 | The wire-wrapping board and the slipknot fabrication process. a, The wire-wrapping board is utilized for pre-tightening slipknots. **b, c**, Based on the pre-tightening status, the slipknot undergoes tension using Zwick/Roell Z010 testing machine until a predetermined force load is achieved. **d**, The sliding knot is gradually pulled apart. **e**, The slipknot is opened as the test machine pulls on both ends of the slipknot. Given the transparent properties of fluorocarbon monofilaments, we use black filaments to enhance visibility during the demonstration.

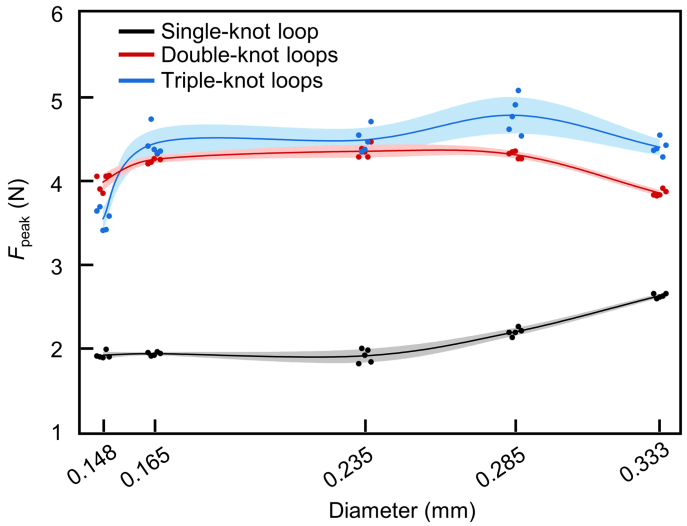

Extended Data Fig. 2 | The relationship between F_{peak} and the thickness of suture. F_{tying} = 5.000 N, pulling speed = 50 mm min^{-1}. F_{peak} is reported as mean ± s.d., based on 5 independent samples.

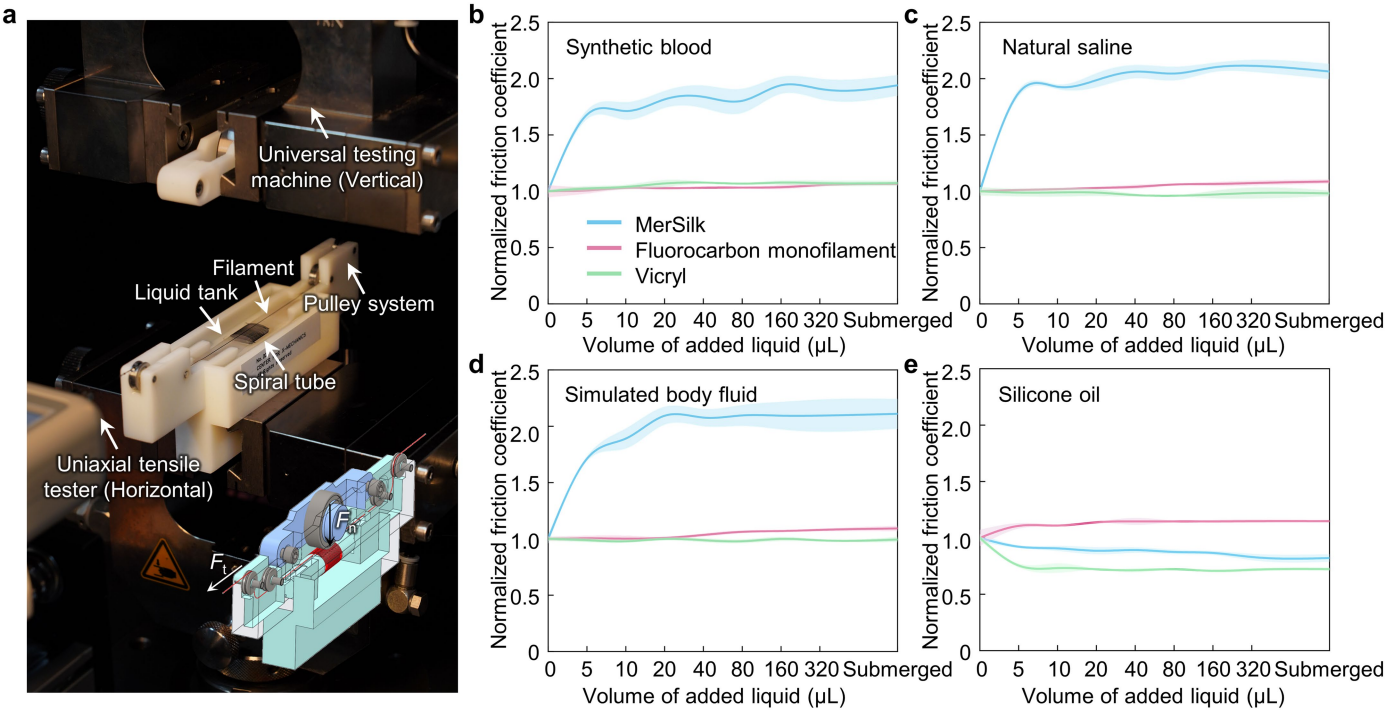

Extended Data Fig. 3 | Measurement of the friction coefficient of filaments in moist and lubricated conditions. a, The filament friction measurement setup in liquid environments. The pulley system allows the filament to be immersed in the tank with varying amounts of liquid. The testing machine (vertical) applies a normal force, F_n, pressing the filament firmly against a spiral tube wrapped with a single layer of the same filament. The testing machine (horizontal) pulls the single filament steadily, allowing the measurement of the tangential force, F_t. **b**–**e**, Normalized friction coefficient of Mersilk, fluorocarbon monofilament, and Vicryl in various volumes of (**b**) synthetic blood, (**c**) natural saline, (**d**) simulated body fluid, and (**e**) silicone oil (mean ± s.d.; ribbons indicate the s.d.; $n = 7$ independent experiments).

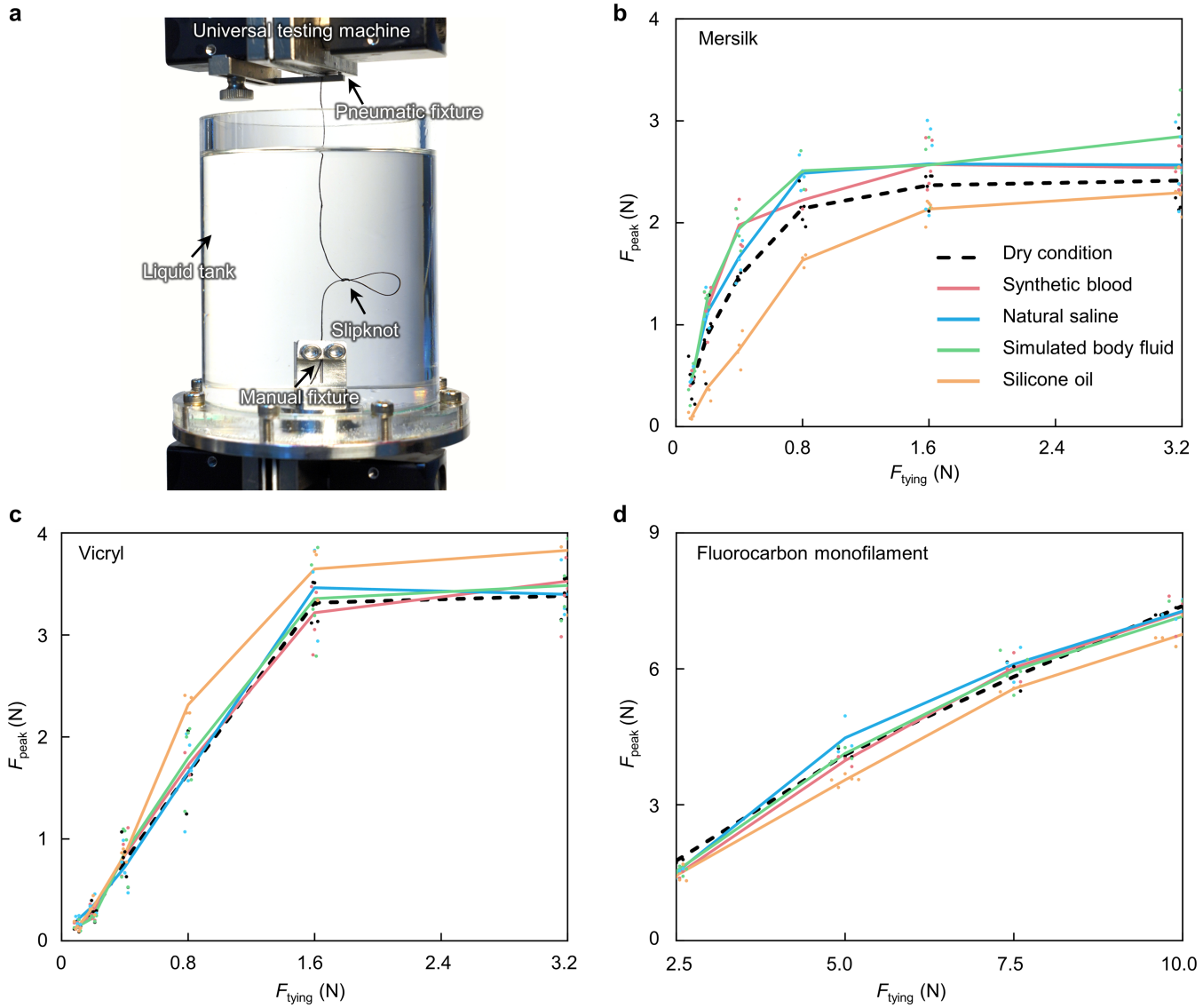

Extended Data Fig. 4 | Measurement of the relationship between F_{peak} and F_{tying} of sliputures in dry, moist and lubricated conditions. a, The uniaxial stretching setup in liquid environments. The manual fixture at the bottom presses the sliputure into the groove and is screwed into the pre-threaded section in the liquid tank to ensure coaxiality during the tensile test. The upper and lower fixtures are brought as close as possible before starting the test to minimize the effect of buoyancy. **b**, The relationship between F_{peak} and F_{tying} for sliputure made with Mersilk in synthetic blood, natural saline, simulated body fluid, and silicone oil. **c**, The relationship between F_{peak} and F_{tying} for sliputure made with Vicryl in synthetic blood, natural saline, simulated body fluid, and silicone oil. **d**, The relationship between F_{peak} and F_{tying} for sliputure made with fluorocarbon monofilament in synthetic blood, natural saline, simulated body fluid, and silicone oil (mean and data points; $n = 3–5$ independent experiments).

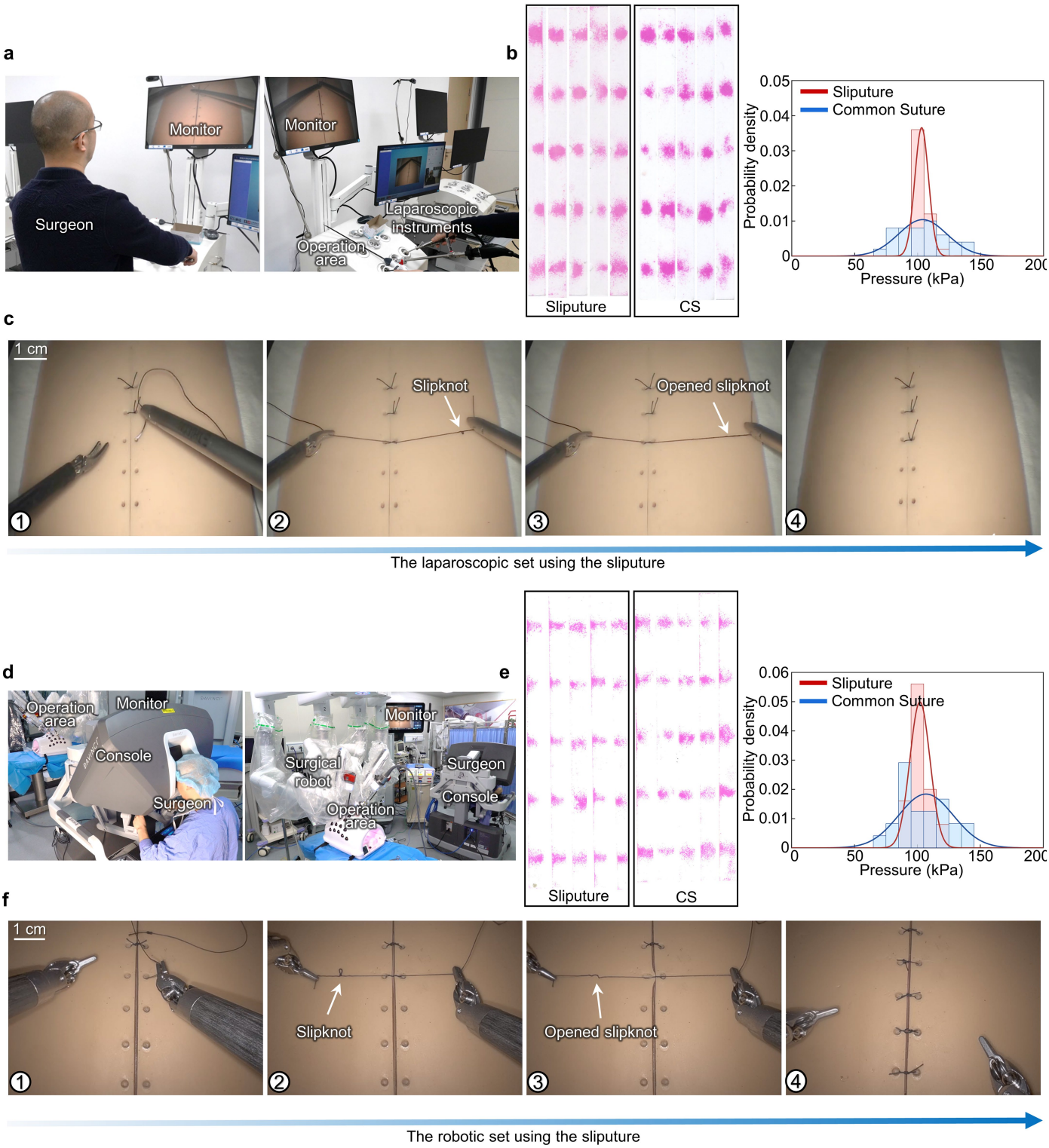

Extended Data Fig. 5 | The incision pressure test of the slipknot under laparoscopic and robotic set. a, The laparoscopic incision pressure test platform. **b**, The result of the pressure-sensitive film shows that the incision pressure of the sliputure group is more concentrated than that of the common suture in laparoscopic set ($V_{\sigma}^{\text{Sliputure}} = 0.054$, $V_{\sigma}^{\text{Common Suture}} = 0.188$) ($n = 25$; independent experiments). **c**, The processing of using the sliputure under laparoscopic set. **d**, The robotic incision pressure test platform. **e**, The result of the pressure-sensitive film shows that the incision pressure of the sliputure group is more concentrated than that of the common suture in the robotic set ($V_{\sigma}^{\text{Sliputure}} = 0.080$, $V_{\sigma}^{\text{Common Suture}} = 0.207$). **f**, The processing of using the sliputure under the robotic set. CS, Common suture.

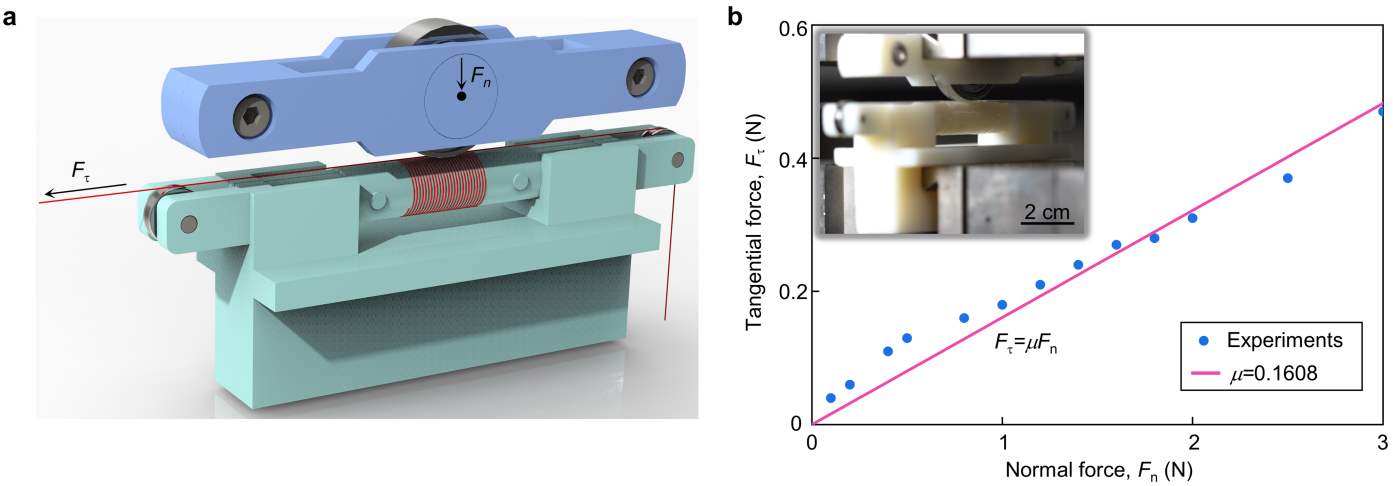

Extended Data Fig. 6 | Fixture for measuring the friction coefficient of strings. a, The assembly diagram of the friction measurement device illustrates a bearing applying a normal force, F_n, to a fluorocarbon monofilament, pressing it firmly against a helical tube wrapped with a single layer of fluorocarbon monofilament. By employing a universal testing machine to pull out the single filament steadily, tangential force, F_τ, can be measured. Photographs show the operating state of the setup. **b**, By measuring the force F_τ under different normal forces F_n and performing a linear fit, the kinematic friction coefficient between the fluorocarbon monofilaments can be determined (n = 13; independent experiments).

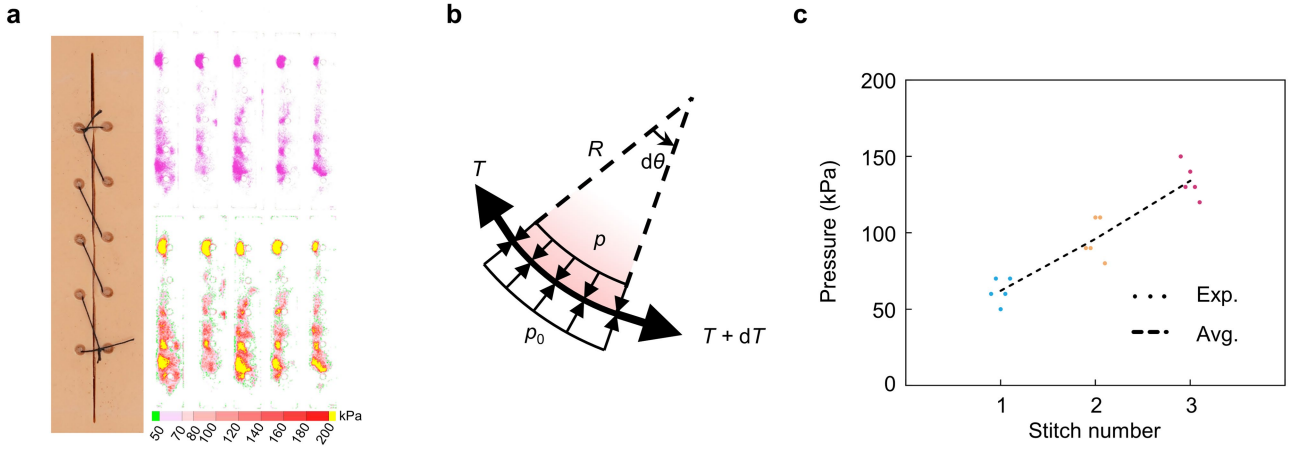

Extended Data Fig. 7 | Incision pressure measurement for continuous sutures of 5 stitches. a, The pressure distribution of a wound closed by continuous sutures. **b**, The scheme of the incision pressure analysis model. **c**, Quantified incision pressure for the middle 3 stitches extracted from the films ($n = 5$; independent experiments).

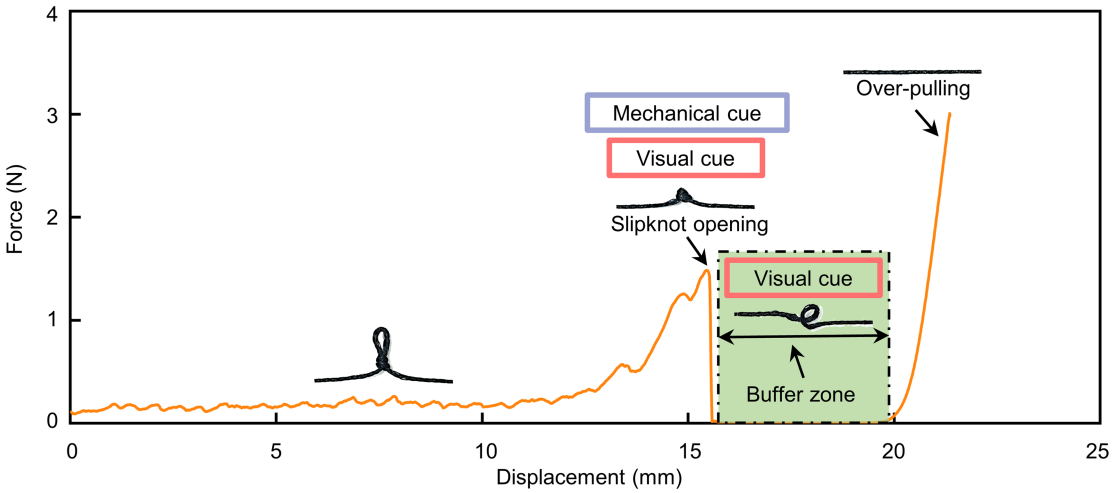

Extended Data Fig. 8 | Force–displacement curve of sliputure. When the slipknot is opened, a redundant length of sliputure is deployed, forming a "buffer zone" where the loading force remains null. This configuration provides both mechanical and visual cues.

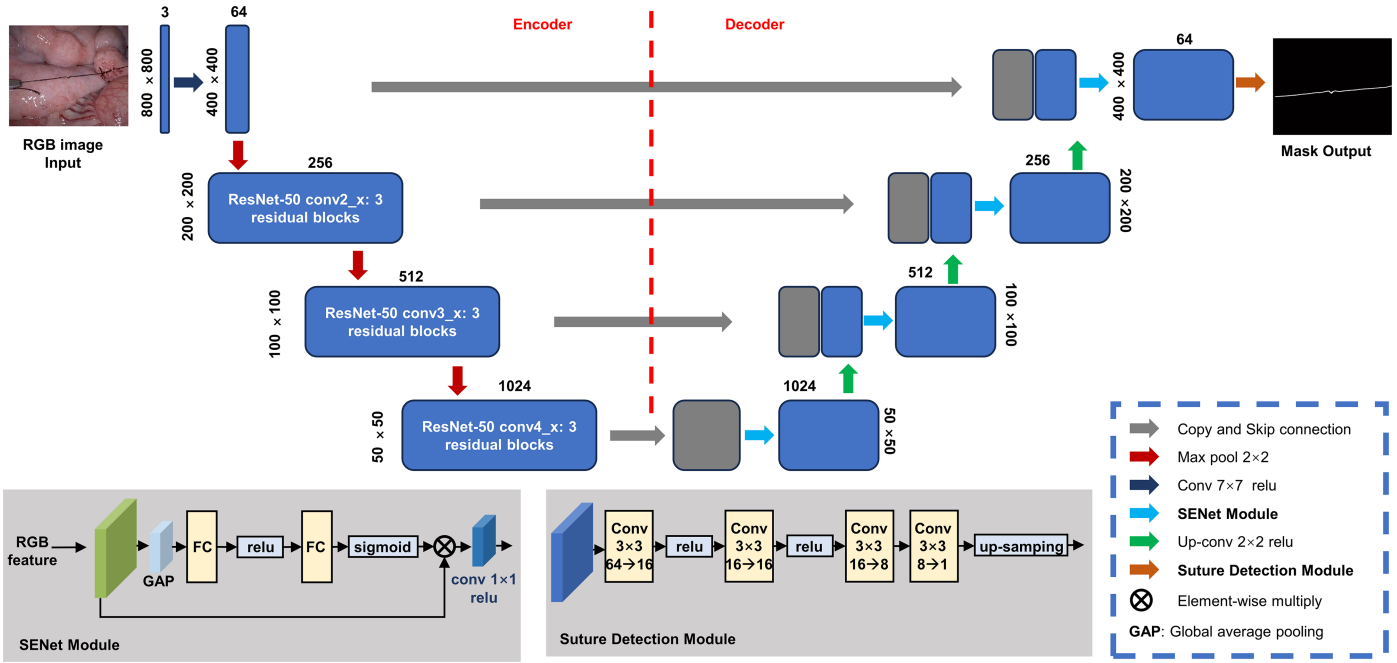

Extended Data Fig. 9 | The architecture of the proposed SlipknotNet. It is an encoder-decoder neural network, in which the image encoder is realized by pretrained ResNet50 and the decoder contains up-convolution operators, SENet modules, and a suture detection module.

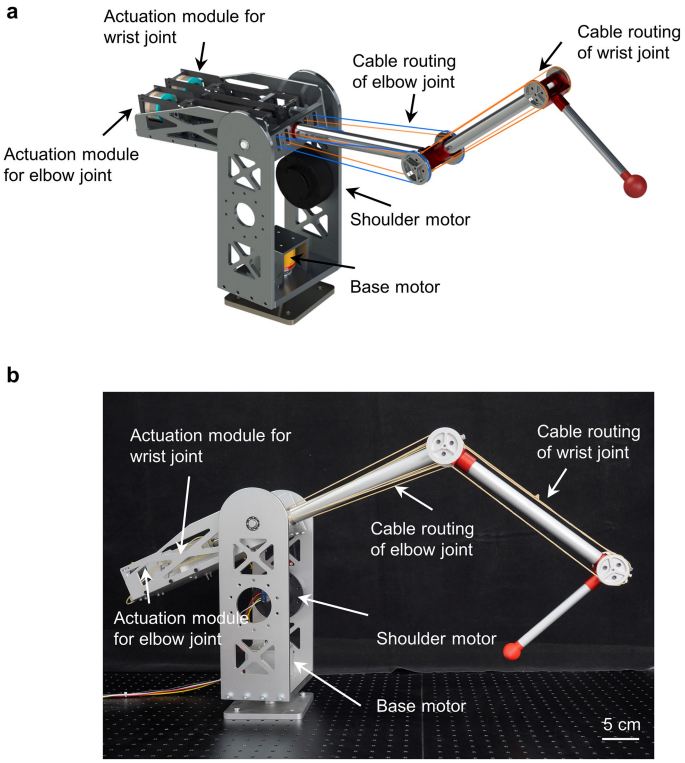

Extended Data Fig. 10 | The slipknot-integrated tendon-driven robotic arm. **a**, A 3D model rendering of the robotic arm. The configuration includes an actuation module for elbow joint, an actuation module for wrist joint, a cable routing of elbow joint, a cable routing of wrist joint, a shoulder motor and a base motor. **b**, The optical picture of the slipknot-integrated tendon-driven robotic arm.

nature portfolio

Corresponding author(s): Tiefeng Li

Last updated by author(s): Aug 27, 2025

Reporting Summary

Nature Portfolio wishes to improve the reproducibility of the work that we publish. This form provides structure for consistency and transparency in reporting. For further information on Nature Portfolio policies, see our Editorial Policies and the Editorial Policy Checklist.

Statistics

For all statistical analyses, confirm that the following items are present in the figure legend, table legend, main text, or Methods section.

n/a	Confirmed
☐	☒ The exact sample size (*n*) for each experimental group/condition, given as a discrete number and unit of measurement
☐	☒ A statement on whether measurements were taken from distinct samples or whether the same sample was measured repeatedly
☐	☒ The statistical test(s) used AND whether they are one- or two-sided *Only common tests should be described solely by name; describe more complex techniques in the Methods section.*
☐	☒ A description of all covariates tested
☐	☒ A description of any assumptions or corrections, such as tests of normality and adjustment for multiple comparisons
☐	☒ A full description of the statistical parameters including central tendency (e.g. means) or other basic estimates (e.g. regression coefficient) AND variation (e.g. standard deviation) or associated estimates of uncertainty (e.g. confidence intervals)
☐	☒ For null hypothesis testing, the test statistic (e.g. *F*, *t*, *r*) with confidence intervals, effect sizes, degrees of freedom and *P* value noted *Give P values as exact values whenever suitable.*
☒	☐ For Bayesian analysis, information on the choice of priors and Markov chain Monte Carlo settings
☒	☐ For hierarchical and complex designs, identification of the appropriate level for tests and full reporting of outcomes
☒	☐ Estimates of effect sizes (e.g. Cohen's *d*, Pearson's *r*), indicating how they were calculated

Our web collection on statistics for biologists contains articles on many of the points above.

Software and code

Policy information about availability of computer code

Data collection	CaseViewer version 2.4 Laser Speckle Contrast Imaging System RFLSI III version 4.0 FUJI film FPD-8010E version 2.5.0.3 Tracker version 6.0.9
Data analysis	GraphPad Prism version 9.5.0 Thermo Science Amira 3D version 2021.1

For manuscripts utilizing custom algorithms or software that are central to the research but not yet described in published literature, software must be made available to editors and reviewers. We strongly encourage code deposition in a community repository (e.g. GitHub). See the Nature Portfolio guidelines for submitting code & software for further information.

Data

Policy information about availability of data

All manuscripts must include a data availability statement. This statement should provide the following information, where applicable:

- Accession codes, unique identifiers, or web links for publicly available datasets
- A description of any restrictions on data availability
- For clinical datasets or third party data, please ensure that the statement adheres to our policy

All data supporting the findings of this study are provided in the paper, the Extended Data figures, and the Supplementary Information. Source data underlying the figures are available on GitHub at https://github.com/Slipknot-Gauged.

Research involving human participants, their data, or biological material

Policy information about studies with human participants or human data. See also policy information about sex, gender (identity/presentation), and sexual orientation and race, ethnicity and racism.

Reporting on sex and gender	Participant selection was based solely on suitability for the research objectives, without consideration of sex or gender. Sex or gender information of participating surgeons was self-reported. For the knot-tying force test, 10 junior surgeons (9 male, 1 female) and 5 senior surgeons (all male) were recruited. For the bimanual knot-tying force test and the incision pressure test of standing sutures, 5 junior surgeons (3 male, 2 female) and 5 senior surgeons (all male) were recruited for each.
Reporting on race, ethnicity, or other socially relevant groupings	Participant selection was based solely on suitability for the research objectives, without consideration of race, ethnicity, or other socially relevant groupings for any of the tests, and no such data were self-reported by participants.
Population characteristics	For the knot-tying force test, surgeons are ranging in age from 23 to 44 years participated in this study. For the bimanual knot-tying force test and the incision pressure test of standing sutures surgeons are ranging in age from 28 to 45 years participated in this study.
Recruitment	All participating surgeons were randomly recruited without bias from the Department of General Surgery, Sir Run Run Shaw Hospital, Zhejiang University School of Medicine, Hangzhou, China. Junior surgeons were defined as those with less than 10 years of clinical experience, and senior surgeons as those with more than 10 years of clinical experience. All participants met the eligibility criteria. In the initial submission, 10 junior surgeons and 5 senior surgeons were randomly selected and recruited for testing. During the revision process, 5 junior surgeons and 5 senior surgeons were randomly recruited to perform the updated tests.
Ethics oversight	Ethics for the study was approved by the Institutional Review Board of Sir Run Run Shaw Hospital, Zhejiang University (Approval No. 2023-0528 and 2025-0023).

Note that full information on the approval of the study protocol must also be provided in the manuscript.

Field-specific reporting

Please select the one below that is the best fit for your research. If you are not sure, read the appropriate sections before making your selection.

☒ Life sciences ☐ Behavioural & social sciences ☐ Ecological, evolutionary & environmental sciences

For a reference copy of the document with all sections, see nature.com/documents/nr-reporting-summary-flat.pdf

Life sciences study design

All studies must disclose on these points even when the disclosure is negative.

Sample size	No formal sample size calculation was performed, and the number of samples was determined by the maximum available resources. In animal experiments exploring the feasible force range, a sample size of n = 20 was used. For ex vivo and in vivo rat colonic defect repair, the sample sizes were n = 5 for ex vivo and n = 5 for in vivo experiments. For comparison of anastomotic complications, the sample sizes were n = 10 in the sliputure group and n = 10 in the control group. For comparison of wound healing, the sample sizes were n = 3 for each subgroup from D1–D8 in both the sliputure and control groups. Laparoscopic and robotic experiments were conducted with a minimum of one pig per group. No statistical methods were applied to calculate sample size.
Data exclusions	Data exclusion was considered when animals appeared sick.
Replication	Unless otherwise specified in the manuscript, all experiments were performed at least three times, either as replications or independent trials, and all replication results were confirmed to fall within the acceptable error range.
Randomization	The animal samples prepared by the same method were randomly allocated to each group.
Blinding	The data were not blinded. The same investigator conducted both the experimental and data analyses; therefore, blinding was not feasible.

Reporting for specific materials, systems and methods

We require information from authors about some types of materials, experimental systems and methods used in many studies. Here, indicate whether each material, system or method listed is relevant to your study. If you are not sure if a list item applies to your research, read the appropriate section before selecting a response.

Materials & experimental systems

n/a	Involved in the study
☐	☒ Antibodies
☒	☐ Eukaryotic cell lines
☒	☐ Palaeontology and archaeology
☐	☒ Animals and other organisms
☒	☐ Clinical data
☒	☐ Dual use research of concern
☒	☐ Plants

Methods

n/a	Involved in the study
☒	☐ ChIP-seq
☒	☐ Flow cytometry
☒	☐ MRI-based neuroimaging

Antibodies

Antibodies used	Anti-CD86 Rabbit mAb (Clone: E5W6H, 19589S, CST, 1:400), Anti-CD206 Mouse mAb (Clone: 2A6A10, 60143-1-ig, Proteintech, 1:5000).
Validation	All antibodies were validated by the manufacture. The details were shown at the manufacture's websites as indicated below: Anti-CD86 Rabbit mAb (19589S, CST, 1:400): https://www.cellsignal.cn/products/primary-antibodies/cd86-e5w6h-rabbit-mab/1958, Anti-CD206 Mouse mAb (60143-1-ig, Proteintech, 1:5000): https://www.ptgcn.com/products/MRC1-Antibody-60143-1-Ig.htm.

Animals and other research organisms

Policy information about studies involving animals; ARRIVE guidelines recommended for reporting animal research, and Sex and Gender in Research

Laboratory animals	The study animals were: SPF (specific pathogen free) rats weighing 200 - 250 g, female, species: Sprague-Dawley rats, age: 4 weeks. Pigs weighing 23 - 27 kg, female, species: Bama miniature pig, age: 5 - 6 months.
Wild animals	No wild animals were used in the study.
Reporting on sex	All animals were female.
Field-collected samples	No field collected samples were used in the study.
Ethics oversight	The animal study was approved by the Institutional Animal Care and Use Committee at Zhejiang University (Approval No. ZJU20230084 and ZJU20250067).

Note that full information on the approval of the study protocol must also be provided in the manuscript.

Plants

Seed stocks	N/A
Novel plant genotypes	N/A
Authentication	N/A